BRNO UNIVERSITY OF TECHNOLOGY
CENTRAL EUROPEAN INSTITUTE OF TECHNOLOGY

VYSOKÉ UČENÍ TECHNICKÉ V BRNĚ
STŘEDOEVROPSKÝ TECHNOLOGICKÝ INSTITUT

UTILIZATION OF POROUS ANODIC ALUMINA FOR FABRICATION OF NANOSTRUCTURED LAYERS AND THEIR PHOTOELECTROCHEMICAL AND OPTICAL APPLICATIONS

VYUŽITÍ PORÉZNÍ ALUMINY PRO PŘÍPRAVU NANOSTRUKTUROVANÝCH VRSTEV A JEJICH FOTOELEKTROCHEMICKÉ A OPTICKÉ APLIKACE

SUMMARY OF DOCTORAL THESIS
TEZE DISERTAČNÍ PRÁCE

AUTHOR
AUTOR PRÁCE
Ing. TOMÁŠ LEDNICKÝ

SUPERVISOR
VEDOUCÍ PRÁCE
Dr. techn. Ing. MÁRIA BENDOVÁ

BRNO 2021

ABSTRACT

Porous anodic alumina (PAA) is an oxide layer formed by anodic oxidation of aluminium. In addition to its vast industrial use, its popularity has exponentially expanded into the field of nanotechnology due to the discovery of the self-ordering growth of PAA, leading to a honeycomb-like nanostructure. Together with a simple fabrication and tuneable properties, PAA represents an inexpensive alternative to the nanoscale world. In the same spirit, this PhD thesis deals with methods utilizing the PAA to fabricate functional nanostructures.

The first part of the thesis is focused on the PAA-assisted formation of titanium dioxide (TiO_2) nanocolumn arrays and their possible application as photoanodes for the water-splitting reaction. TiO_2 nanocolumns are formed by anodisation of superimposed Al layer over titanium substrate being so-called 'PAA-assisted anodisation'. The present study demonstrates the electrochemical properties and photoelectrochemical performance of nanocolumns formed from nitrogen-enriched substrates modified by various thermal treatments. The major finding was that their hollow morphology causes their poor performance. This issue was addressed by developing a novel anodising strategy that originates from the extensive study of anodising parameters and their effect on the morphology and stability of nanocolumns.

The second part demonstrates the fabrication of well-ordered gold nanoparticles (AuNPs) on a transparent substrate as a localized surface plasmon resonance (LSPR) sensor element. A key-stone of this multidisciplinary method is a combination of a self-ordering behaviour of PAA that produces the template for controlled solid-state dewetting (SSD) of a subsequently deposited thin film of gold. This work includes the detailed technical aspects of complete fabrication, starting with the template production from an aluminium sheet to forming AuNPs and their transfer to a transparent substrate. This part is concluded with the characterization of fabricated AuNP nanocomposites with a practical comparison of their bulk refractive index sensitivity and stability in time. Results show this large-scale and inexpensive technique can easily compete with other, more demanding, AuNP fabrication technologies.

KEYWORDS

porous anodic alumina, fabrication, nanostructures, titanium dioxide, gold nanoparticles, photoelectrochemistry, localized surface plasmon resonance.

ABSTRAKT

Porézní anodická alumina (PAA) je oxidová vrstva vytvořená anodickou oxidací hliníku, která má široké průmyslné využití. Její popularita zaznamenala exponenciální nárůst zejména v oblasti nanotechnologií, k čemu přispělo objevení jejího samouspořádání do struktury o nanorozměrech připomínající včelí plástev. Její jednoduchá příprava a laditelné vlastnosti z ní tvoří levný způsob výroby nanostruktur. Ve stejném duchu se tato disertační práce zabývá metodami přípravy funkčních nanostruktur za využití PAA.

První část je zaměřena na výrobu pole nanosloupců z oxidu titaničitého (TiO_2) a jejich možné použití jako fotoanody pro štěpení vody. TiO_2 nanostloupce jsou tvořeny anodizací hliníkové vrstvy na titanovém substrátu, také nazývanou PAA-asistovaná anodizace. Táto studie demonstruje elektrochemické vlastnosti a fotoelektrochemickou aktivitu nano sloupců vytvořených z dusíkem obohacených substrátů, které byly následně různě termálně modifikovány. Hlavním poznatkem studie je, že špatné vlastnosti jsou způsobeny dutou morfologií nanosloupců. Tento poznatek vedl k rozsáhle studii zabývající se dopadem anodizačných podmínek na morfologii ale i stabilitu vytvořených nanosloupců, jejímž výsledkem byla nová strategie anodizace.

Druhá část prezentuje výrobní proces přípravy uspořádané vrstvy zlatých nanočástic na transparentním substrátu pro jejich použití jako optického senzoru využívající efekt rezonance lokalizovaných povrchových plasmonů. Základem této multidisciplinární metody je využití kombinace samouspořádání PAA k výrobě šablony a následného procesu řízeného smáčení v pevné fázi tenké vrstvy zlata. Táto práce detailně popisuje technologické aspekty přípravy; od samotné výroby šablon z hliníku, přes vytváření zlatých nanočástic, až po jejich přenos na transparentní substrát. Na závěr této práce jsou kompozity z nanočástic charakterizovány, přičemž je porovnána jejich citlivost na změnu indexu lomu okolí a jejich stálost. Ze závěrů vyplývá, že tato poměrně velkoplošná a levná metoda je konkurence schopná i v oblasti senzorické citlivosti.

KLÍČOVÁ SLOVA

porézní anodická alumina, výroba, nanostruktury, oxid titaničitý, zlaté nanočástice, photoelektrochemie, rezonance lokalizovaných povrchových plasmonů.

LEDNICKÝ, Tomáš. *Utilization of porous anodic alumina for fabrication of nanostructured layers and their photoelectrochemical and optical applications*. Brno, 2021. Available also at: https://www.vutbr.cz/studenti/zav-prace/detail/135699. Doctoral Thesis. Vysoké učení technické v Brně, Středoevropský technologický institut VUT, Central European Institute of Technology BUT. Supervisor Mária Bendová.

ACKNOWLEDGEMENT

I would like to express my gratitude to my supervisor Dr. Mária Bendová who gave me this opportunity. I am thankful for her supervision, kind attitude, support, and handful of patience while teaching me more systematic approach through my stubbornness. My sincere gratitude and enormous respect go to Dr. Attila Bonyár (BUTE, Hungary) who unconditionally joined this journey with his endless support, enthusiasm, and especially his never-ending trust in me. Moreover, I am profoundly grateful for his help on this work; his hard-working and humble attitude that has been always an ideal inspiration for me.

The results in this thesis reflect several collaborations I have been lucky to take part in. In addition to the one with Dr. Attila Bonyár, I am grateful to Prof. Achim Walter Hassel for his opportunity to do an internship in his group at Johannes Kepler University Linz. I would like to thank Dr. Andrei Ionut Mardare for his help with my integration during the stay, and Michael Pichler for his technical support. Moreover, I am grateful to Dr. Jan Macák for possibility to do some measurements in his labs in Pardubice, and even more to Dr. Miloš Krbal for doing them.

I would like to thank all my colleagues who not only helped me directly or indirectly but also created a joyful scientific ground for work. Namely, my friend Dr. Radim Zahradníček who was always ready to give all of his ideas, solutions and give his best in table tennis matches. Then, Dr. Ondřej Man for his useful consultations, Dr. Lukáš Flajšman, Dr. Alexandr Otáhal and Jakub Sadílek for their advice and broad technical help. This way I would also like to express my gratitude to CEITEC staff, members of the former Labsensnano research group, and especially members of Nano Research Infrastructure for doing their best to keep machines in the operating state and making the research more accessible.

Personally, I would like to thank Dr. Milena Setka who managed to survive few last years with me in the office and did not go crazy. For similar accomplishments and revision of this work, a big thanks goes to my friend and roommate Dr. Štepan Kuchař. I would like to thank all my friends for their enriching company outside of science and their persistent nagging about the period of my PhD study. Last but not least, from the bottom of my heart I would like to thank my family and especially my parents, who supported me from the very beginning.

I also thank the funding agencies who supported this work. The internship was supported by Erazmus+ program of European Union, part of the work was carried out with the support of CzechNanoLab infrastructure (ID LM2018110, MŠMT, 2020–2022), CEITEC Brno University of Technology, and part of the research leading to the presented results has been supported by the Czech Science Foundation (GAČR) project no. 15-23005Y.

CONTENTS

1 PHOTOELECTROCHEMISTRY ON TIO_2 NANOSTRUCTURES

Titanium dioxide (TiO_2) is well known to be the most practical and prevalent photocatalyst, for it is chemically stable, abundant, nontoxic, and cost-effective. The appropriate electronic band structure and excellent surface activity endow TiO_2 with promising potential in hydrogen production, photovoltaics, photocatalysts, lithium-ion batteries, fuel cells, gas sensors, detoxification, and supercapacitors. These applications can be roughly divided into 'energy' and 'environmental' categories. Although TiO_2 possesses such a promising potential, its relatively poor charge transport property and wide bandgap (3.0–3.2 eV), which can utilise only a fraction of the available solar energy (5–7 %), are the two main limitations for its application in catalysis and energy harvesting. Therefore, in recent years, many scientists dedicated their work to overcome these limits. It is no surprise that TiO_2-related materials have been a 'hot' topic of a vast amount of scientific research focused on their formation [1, 2], properties [3, 4], and applications [5, 6], which is proven by multiple excellent reviews dedicated to the TiO_2 topic.

1.1 Motivation and aims of the work

In recent years, TiO_2 nanostructures became a hot topic to benefit from increased surface area and decreased bulk volume. Among other techniques (e.g., hydrothermal, sol-gel, physical/chemical vapour deposition), the synthesis of nanotubes/nanopores by anodic oxidation of titanium, an analogy to the PAA fabrication, became the most popular and deeply studied.[2, 7] Despite its popularity, the synthesis requires an aggressive fluorine-based solution that contaminates the titanium nanotubes by fluorine ions and represents an additional safety hazard during the fabrication process. In these regards, the PAA-assisted anodisation (discussed in the previous section) presents a more convenient and environmentally friendly alternative for fabricating TiO_2 nanostructures.

However, compared to the titanium nanotubes (TNTs), this area is barely explored, as can be evident by no reports studying the electrical or photoelectrical properties of these TiO_2 nanocolumns (except for one conference paper [8] from our group). One of the reasons may originate from the difficulty of forming stable and reasonably high nanocolumn arrays. Such an unexplored and challenging area greatly motivates this work to investigate further the fabrication process and properties of TiO_2 nanocolumns formed by this unconventional anodising technique.

As for most TiO_2-based nanomaterials, the ultimate goal is to develop a photo-anode material that can be utilised in solar energy harvesting and water splitting applications. The photocatalytic performance of nanocolumns should be enhanced by minimising the drawbacks of TiO_2, which are the relatively wide bandgap and poor electrical properties. In the literature, two approaches are frequently used to decrease the bandgap of TiO_2

and change its photocatalytic activity towards visible light absorption: i) doping TiO_2 with different elements (e.g., Nb, Ta, N, C); and ii) thermal treatment of TiO_2 in various environments.

Therefore, the objective is split into several tasks:

(i) The investigation of the electrochemical properties of nanocolumn arrays formed from various compositions of substrate demonstrates the effect of doping, while different thermal treatments prove a positive effect of the phase transition and possible formation of oxygen vacancies.

(ii) The main objective of the work is the study of the photoelectrochemical properties of nanocolumn arrays. This study demonstrates the advantages and possible drawbacks of nanocolumn arrays compared to more common TiO_2 surfaces.

(iii) Later, another objective was added due to adverse outcomes from the last part. It was found that poor nanocolumn stability and hollow morphology present severe obstacles on the way to any significant performance. Therefore, the goal was to obtain better stability for a wide range of nanocolumn arrays (substrates, heights). All this was performed by a systematic study of anodising parameters and their effects on the nanocolumn morphology and stability.

1.2 Porous anodic alumina assisted anodisation

Porous anodic alumina (PAA)-assisted anodisation is the principal fabrication technique used in this part to form nanostructure surfaces. The PAA-assisted anodisation combines the porous anodic oxidation of the aluminium layer with the anodisation of superimposed layers. The substrate (i.e., the underlying layer) is usually another valve metal (e.g., Nb, Ta, Ti, W, Zr). Since the resistivity of the aluminium oxide is in general higher than that of the oxide of the other valve metals, this situation relates to the reversed, unstable circumstances leading to the migration and mixing of the underlying oxide. In contrast to the barrier-type anodising of superimposed layers, the anodised area and the growth of the underlying oxide are confined by the preformed porous mask of the overlying PAA layer. Figure 1.1 illustrates this process. Such a situation is similar to numerous separated barrier-type anodising processes co-occurring at the bottom of each pore, characteristically called the barrier layer, despite a few differences, such as the geometry, chemical composition, and nanosized lateral dimensions. The PAA-assisted anodisation has a similar development in a single pore area compared to its flat analogy.

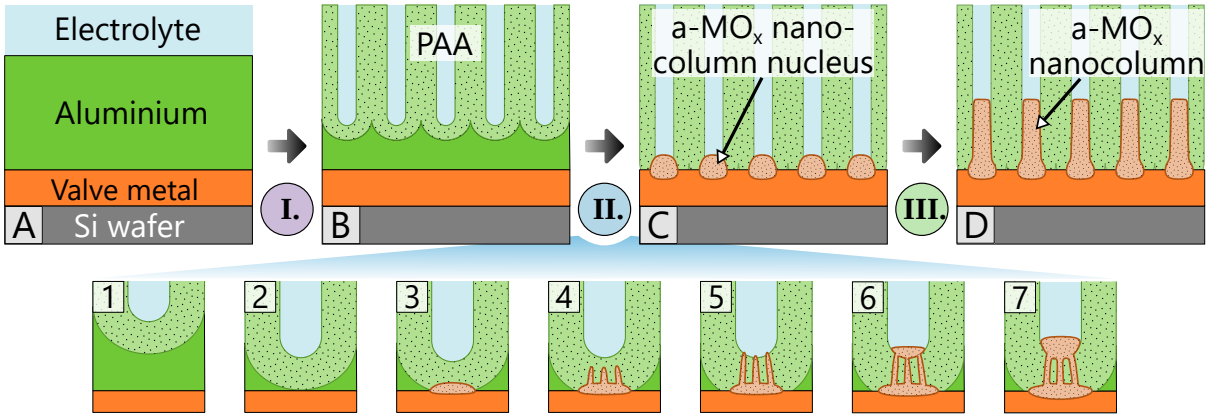

Figure 1.1: Schematic illustration of (A–D) exemplary PAA-assisted anodising of an Al/valve metal bilayer resulting in the formation of PAA-embedded a-MO$_x$ nanocolumns. (1–7) A detailed schematic of an example of nuclei growth. The roman numbers mark anodisation stages (used later in the text and illustrated in Figure 1.3): I.) aluminium anodising, II.) substrate anodising, and III.) substrate re-anodising. Schematic inspired by results in the experimental section (section 1.3).

Figure 1.1 represents a schematic illustration of PAA-assisted anodisation of an aluminium/valve-metal (Al/M) bilayer. During this process, the porous anodising of Al overlayer forms a layer of PAA (Figure 1.1:B). After the whole Al layer is consumed and the PAA reaches the underlying metal layer (Figure 1.1:2), the growth of underlying anodic metal oxide (a-MO$_x$) occurs (Figure 1.1:3). Afterwards, the less resistive substrate oxide penetrates the more resistive barrier layer, possibly in the form of fingers (Figure 1.1:4–5). When the substrate oxide thoroughly penetrates the barrier layer, it may form a cap at

the bottom of the pore (Figure 1.1:6–7). The final structure (Figure 1.1:7), resembling a tooth by its shape, where a part of alumina from the barrier layer is trapped within the a-MO_x structure.

Furthermore, the anodisation process can be extended into the so-called re-anodisation stage (Figure 1.1, stage III.). During this stage, the anodising potential is increased and leads to additional growth of the oxide cap that fills the interior of the pore, inheriting its columnar shape (Figure 1.1:D). Since the thickness of the a-MO_x strongly depends on the formation potential,[9] moderating it provides an excellent method to control the length of oxide structures.

The stability of the whole array can be estimated as the fraction of free-standing columns to all columns. The evaluation is performed from the SEM images (Figure 1.2:A), where free-standing columns are seen as bright spots while broken columns are usually washed away, leaving a much darker root base. Graphs in Figure 1.2:B, C show the esti-

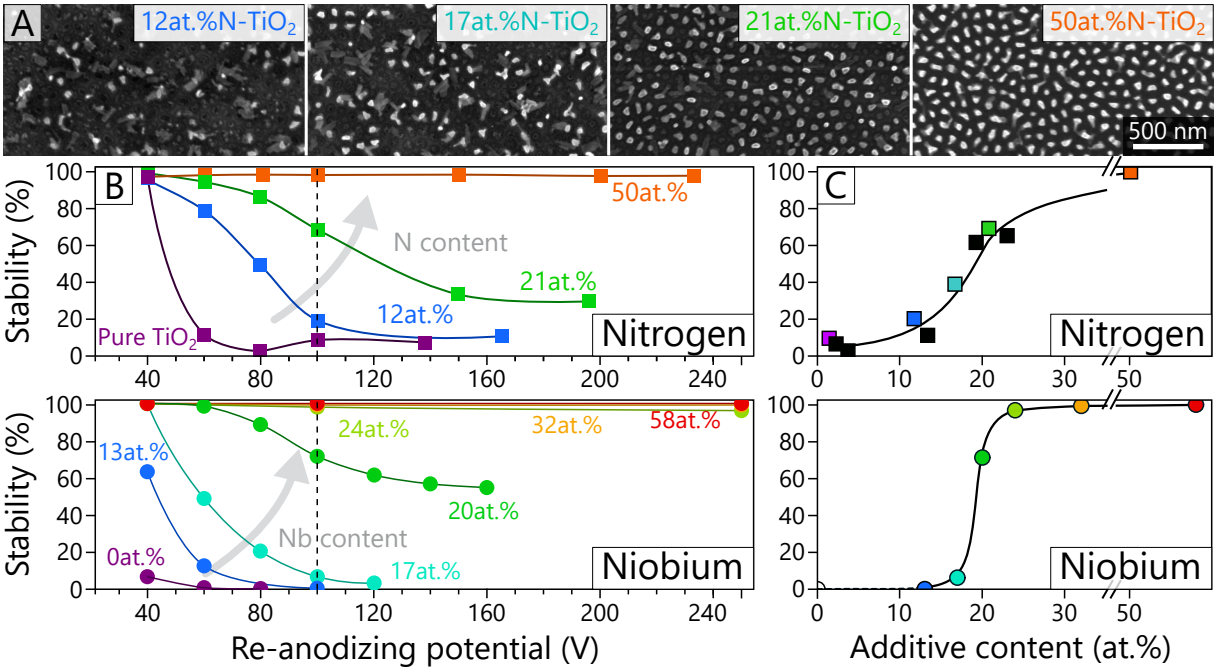

Figure 1.2: A comprehensive summary of the stability of nanocolumns formed from nitrogen and niobium doped substrates and re-anodized to various potentials. Reproduced and adapted with permission from ref. [10, 11].

mated stability of nanocolumn arrays formed on Ti-based substrates of various nitrogen or niobium content and re-anodised to selected potentials. The most important conclusion is that the stability decreases considerably with the increased re-anodising potential, limiting the attainable length of nanocolumns. The studies show that a significant improvement can be achieved by adding nitrogen or niobium into the titanium layer, thus changing the substrate composition. These admixtures improve the stability, and even longer nanocolumns can be obtained for a selected re-anodising potential.

1.3 Experimental, results and discussion

1.3.1 Fabrication of TiO_2 nanocolumn arrays

Anodisation processes were conducted in two technologically different setups: a flow-through pressing cell and a large-scale fabrication setup. As both setups have different pros and cons, their use varies based on the application. While the pressing cell setup can be advantageous in research and development areas such as finding the right anodising conditions, the large-scale fabrication setup can be utilised for high throughput fabrication where good uniformity in each batch is guaranteed.

Substrates

In this work, the titanium oxide nanocolumn arrays were fabricated by the PAA-assisted anodisation of bilayers of superimposed aluminium on a substrate layer based on titanium (oxidised to some degree) with an admixture of nitrogen or niobium. Table 1.1 summarises the bilayers used in this work (the labels representing the fraction of admixture are used for reference in the further text).

Table 1.1: Parameters of bilayers, used in this study, of superimposed aluminium over substrate layer.

Label	Substrate layer	Thickness [nm]		Atomic concentration [%]				
		Al	Substrate	Ti	O	N	C	Nb
Ti	Ti	500	200	not available				
1/5N	$TiO_x N_y$	500	380†	50.6	32.6	9.5	7.4	
1/4N	$TiO_x N_y$	600	200	71.5	0.9	18.2	2.4	
1/3N	$TiO_x N_y$	600	210†	49.8	28.2	16.3	5.8	
1/1N	$TiO_x N_y$	600	405†	40.1	15.4	40.3	4.2	
1/4Nb	$TiO_x Nb_y$	600	150	42.1	32.4	3.3	7.1	10.5

† Value estimated from a SEM measurement. Otherwise estimated from deposition parameters.

All bilayers except 1/4Nb were sputter-deposited (by Dr Imrich Gablech) on 4 inches oxidised Si wafers using an ion-beam sputtering apparatus (Bestec) equipped with a radio frequency inductively coupled plasma (RFICP) Kaufman ion-beam source.[11, 12] 1/4N with the admixture of niobium was sputter-deposited (by Dr Jan Prášek) in the magnetron sputtering system (Bestec, reference) co-sputtering from Ti and Nb targets.

Compositions of substrate layers, tabulated in Table 1.1, were estimated by XPS. Before the analysis, the samples were immersed in an aqueous 0.1 M sodium hydroxide solution to remove the superimposed Al layer. Afterwards, they were cleaned in deionised water (MiliPore, 18.2 MΩ) and dried by a nitrogen stream. Compositions of substrates

were then estimated by XPS analysis. The quantification was performed from broad XPS spectra obtained after several sputtering cycles (Ar^+, 5 keV).

Anodisation in the flow-through pressing cell setup

The flow-through pressing cell (illustrated in Figure 1.3:A) consists of a cylindrical polytetrafluoroethylene (PTFE) body with a silicon o-ring seal (inner diameter of 7 mm) that confines the anodising area. A gold wire coiled around a glass inlet tube is used in this setup as a counter electrode (CE) and a horizontally placed sample as a working electrode (WE). Both electrodes are connected to a source meter by 4-wire sensing (with a current limit of 21 mA, Keithley 2410) controlled through a home-made software interface (Labview). An electrolyte exchange is secured by a membrane pump (KNF SIMDOS 10) with a flow rate of 70 cm min^{-2}.

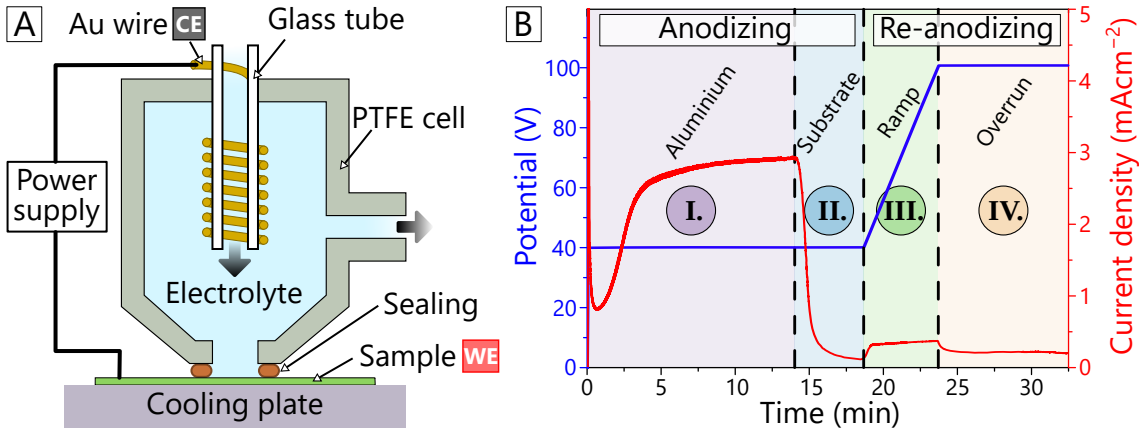

Figure 1.3: (A) Schematic illustration of the flow-through pressing cell during anodisation. (B) A representative example of current density vs time response (red line) during potential-controlled (blue line) anodisation of aluminium/titanium bilayers (Table 1.1: ¼N) in the pressing cell setup.

For this setup, bilayers were processed as received without any additional cleaning or area masking. The wafer was cut to square samples with a side length of at least 10 mm. All anodising processes were performed in a potential controlled regime in a 0.3 M aqueous solution of oxalic acid (Sigma-Aldrich) placed in a reservoir of 500 ml volume and cooled to the desired temperature. Before each anodisation process, the setup (the cell, silicon tubes, and sample) was tempered for at least 5 minutes by electrolyte circulation.

As an advantage of the pressing cell setup, no advanced sample preparation is necessary, which dramatically speeds up the R&D process. Additionally, the WE is well defined, ensuring a reasonable control over the current flowing through the sample and a more straightforward comparison between various anodising methods. In general, disadvantages of the setup include a small WE, non-ideal control of temperature or electrolyte flow, and the CE geometry.

Figure 1.3:B shows the classical behaviour of process parameters (used in this work) during the PAA-assisted anodisation. This process can be divided based on ongoing events (schematically illustrated in Figure 1.1) into four stages: I.) aluminium anodising, II.) substrate anodising, III.) re-anodising ramp and IV.) re-anodising overrun.

First (Figure 1.3:B stage I), the top aluminium layer is porously anodised (Figure 1.1:B). This process is typically done in a potentiostatic mode at 40 V and in 0.3 M oxalic acid to ensure one of the best pore self-ordering. Stage I lasts until the PAA reaches the bottom substrate layer while consuming almost the whole aluminium layer. When stage I ends and stage II starts, a sudden decrease in the current density occurs.

During stage II, two simultaneous events occur; finalisation of the PAA growth causes a significant current density decrease and anodisation of the substrate layer forming initial nanocolumn nuclei at the bottom of pores (Figure 1.1:B stage II). Exponential decay of current density is typical for this stage.

Afterwards , nanocolumn nuclei can be lengthened by a so-called re-anodising process (stage III and IV) characterised by a higher anodising potential. This process is divided into a potentiodynamic and a potentiostatic part. The potentiodynamic regime (stage III) represents a rising linear sweep (ramp) of anodising potential, starting at the PAA formation potential and finishing at the so-called re-anodising potential. Here, nuclei grow in length with the increasing potential accompanied by an increase of the current density. In the next stage (stage IV), the growth of nanocolumns halts when a constant re-anodising potential is applied, which gives a current density decay. During this stage, no further morphological changes are expected; however, findings show this stage may influence the chemical composition or crystal structure within the roots of nanocolumns (as will be discussed in later subsection 1.3.2).

Anodisation in the large-scale processing setup

In contrast to the individual processing limited by the small diameter of the pressing cell (Figure 1.3:A), the large-scale fabrication process was developed to enable the production of large-scale samples as well as to improve the uniformity control over a large sample area. This setup, uses the same large reservoir of the cooled electrolyte, but instead of delivering it through a circulating system to the sample, the sample is directly immersed into it. The setup includes a two-electrode cell with the partly immersed sample as the anode and a stainless-steel mesh (100 cm) as the cathode. Anodisation experiments in this part were conducted in the same electrolyte (0.3 M oxalic acid) cooled to 10 °C and gently stirred by a magnetic stirrer.

This setup allows larger samples with up to 50 cm compared to 0.4 cm for the pressing cell setup. It is beneficial mainly in experiments, which require a perfect uniformity of the batch. A large piece can be anodised all at one and then split into several smaller identical samples, which can undergo various post-anodising processing such as PAA etching or thermal annealing. However, this technique has a few drawbacks. The major one is that

the sample needs special processing by splitting the anodisation into two parts. Due to common parallel parasitic currents through the sample edges or complicated sample area, the anodisation is better suited for potentiostatic control instead of galvanostatic one.

Before anodisation, the wafer with the deposited layers was cut into 40 mm×25 mm pieces, which were backside laser-grooved into four strips of 10-mm width for later dicing.

On the contrary to the previous processing, the anodisation of Al is divided into two steps. The first step (pre-anodising) was conducted with the initial ramp of $5\,\mathrm{V\,s^{-1}}$ from 0 to 40 V and the current limit of 100 mA, followed by a constant 40 V anodising for 200 s. Afterwards, the samples were thoroughly washed in deionised water and dried by an air stream . This purely technological step creates a thin PAA layer that, with an additional strip of Kapton tape, prevents further undesirable soaking of the sample due to wetting with electrowetting and secures a stable processing area (20 mm×10 mm). The second step continues with the Al anodisation at the same potential (40 V). Then, it is followed by substrate anodising starting around the tenth minute (600 s). The re-anodising ramp of $0.2\,\mathrm{V\,s^{-1}}$ to 100 V starts after 5 minutes of substrate anodising, followed by a 5-minute re-anodising overrun. These conditions were the same for all samples of various substrates (⅕N, ⅓N, two pieces of ¹⁄₁N) used for the photoelectrochemical experiments.

Wet etching of PAA

The PAA-assisted anodisation creates an array of anodic metal oxide (a-MO_x) nanostructures still embedded within the PAA template. Such embedded arrays were also the subject of this study (as discussed in the next subsection 1.3.3), although many applications require removing the passive PAA template and revealing the whole active surface of nanocolumns. The increase in the accessible surface is significant. For cylindrical geometry, it is at least 5× and 40× increase for columns with the aspect ratio of 1 and 10, respectively.

After the anodising process, the samples were thoroughly washed in deionised water and dried by a nitrogen stream. The PAA was removed by chemical wet etching in an aqueous solution of 0.42 M phosphoric acid (H_3PO_4) and 0.2 M chromium trioxide (CrO_3) at 65 °C (based on the etching process in ref. [13]). The extent of the PAA removal was controlled by the etching time, after which the samples were quickly washed in water and dried again.

Figure 1.4 shows successful partial removal of the PAA layer, so the nanocolumn arrays of various heights are equally exposed. However, still, numerous overetched sites occur in the PAA. These sites expose the underlying substrate layer to a degree related to the thickness of the remaining PAA and nanocolumn lengths. When the columns get longer, and thus the remaining PAA gets thicker (in the order ⅕N < ⅓N < ¹⁄₁N), the overetching cannot dig through the whole layer for given conditions. In addition to SEM images (Figure 1.4:A, B, C1), this is also proven by the increased current consumption

during the anodisation of these layers, labelled here as the post-anodising. The cross-section of Figure 1.4:C1 (right) captures the depth of an overetched site showing almost complete penetration through the PAA. These overetching sites create a characteristic clover-like feature in the top view of SEM (Figure 1.4:C1).

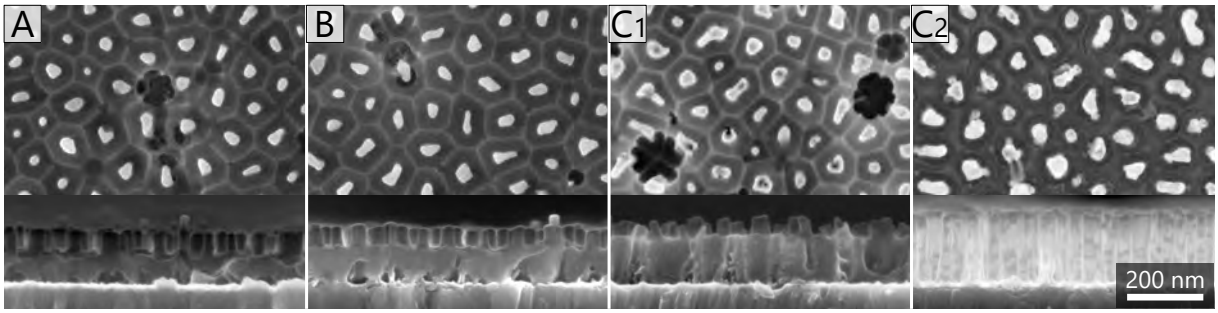

Figure 1.4: SEM images of partly etched (PE) (A) ⅕N, (B) ⅓N, (C1) ¹⁄₁N, and (C2) fully etched (FE) ¹⁄₁N nanocolumn layers. Samples were etched for 23 and 80 min, in the case of PE and FE, respectively. The length of exposed columns is approximately 70 nm for PE ⅕N, ⅓N, and 60 nm for PE ¹⁄₁N layers. The thickness of remaining alumina layer was estimate to 80, 110, and 140 nm for ⅕N, ⅓N, and ¹⁄₁N layers, respectively. The length of FE ¹⁄₁N nanocolumns is approximately 190 nm.

1.3.2 Morphology and stability of nanostructures

The previous section describes the fabrication process of titanium oxide nanocolumns by the PAA-assisted anodising of an aluminium layer superimposed over a substrate layer. This section further focuses on the vast possibilities of how to influence their morphology, structure, or even their chemical stability. The stability drops significantly with increasing titanium purity, thus decreasing the concentration of additives (nitrogen [11], niobium [10]) in the substrate layer and increasing re-anodising potential. Overall, these results demonstrate that the selected anodising conditions will not yield a stable column layer re-anodised to over 100 V for substrate layers with low concentrations of additives (<20 at.% of nitrogen [11] or niobium [10]). Sadly, it limits the potential length of columns, decreases their active surface area, and reduces their competitiveness in possible applications.

These unfavourable findings motivate the following study focused on the effect of anodising parameters on the stability of nanocolumn arrays. The main goal is to achieve a perfect or at least better stability for nanocolumn arrays of various column lengths deriving even from substrates with a low concentration of additives (N, Nb).

The most crucial improvements of stability were achieved by lowering the electrolyte temperature and shortening the re-anodising period. A general rule to form stable TiO_2-based a-MO_x columns by the PAA-assisted anodisation is to promote fast changes of potential, and thus fast kinetics of anodising. Vice versa, this may be interpreted as to avoid idling at any given formation state, such as too long substrate anodising, slow re-anodising, or even prolonging the redundant overrun period, as shown in Figure 1.5.

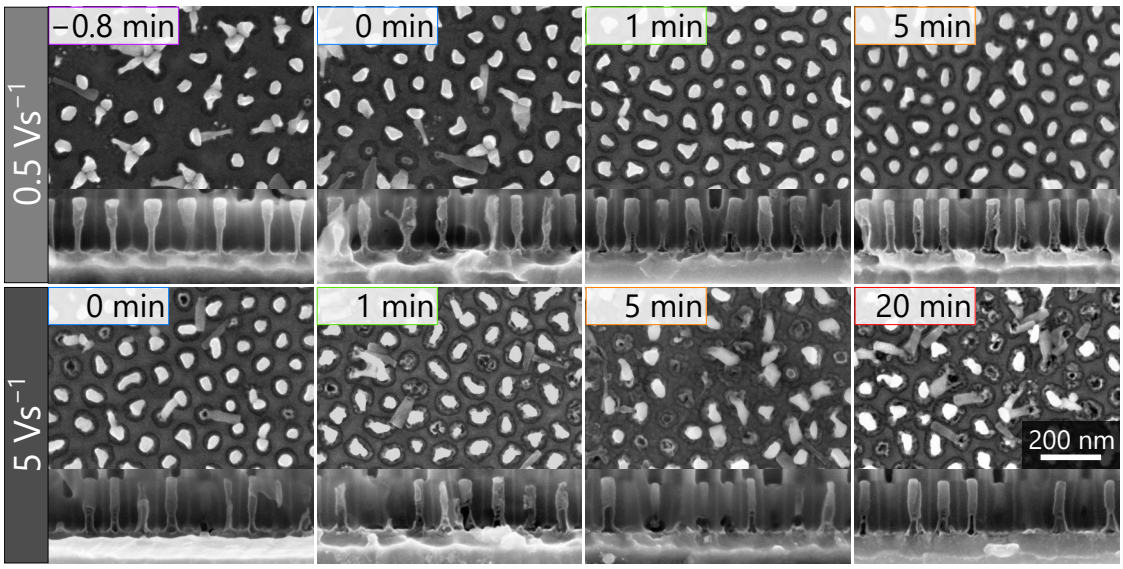

Figure 1.5: Top and cross-view SEM images of (top) PAA-free and (cross-view) PAA-embedded nanocolumn arrays formed by PAA-assisted anodising of ¼Nb substrate. After **substrate anodising** for −0.8, 0, 1, 5, and 20 min, the sample was re-anodised to **100 V** with **0.5 Vs^{-1}** and **5 Vs^{-1}** ramp sweep and a 1-minute overrun period.

Significant attention was paid to the morphology of nanostructures depending on the anodising conditions as it plays a significant role in the overall stability of columns together with the chemical composition of their roots. Two features are correlated with their relatively poor stability: a narrow root formed by the early starts of potential sweep and a large root area associated with a prolonged period of the anodising stage. The anodising periods such as re-anodising ramp and overrun can be reduced to a minimum without any profound impact on the columns. However, in the case of the substrate anodising period, the situation is more complex. Short periods result in narrow roots or even more dramatic morphology changes of the whole column into the saguaro-like shape, while too long periods yield the undesirable root broadening, as shown in Figure 1.6. Nevertheless, these edge conditions still give a reasonable operating window, which may be broadened by lowering the temperature. Surprisingly, the saguaro-like shape columns have superior stability compare to normal (cylindrical) ones formed under similar conditions. Possible drawbacks are some loss of the active surface due to merging in the trunk and getting a more complex shape.

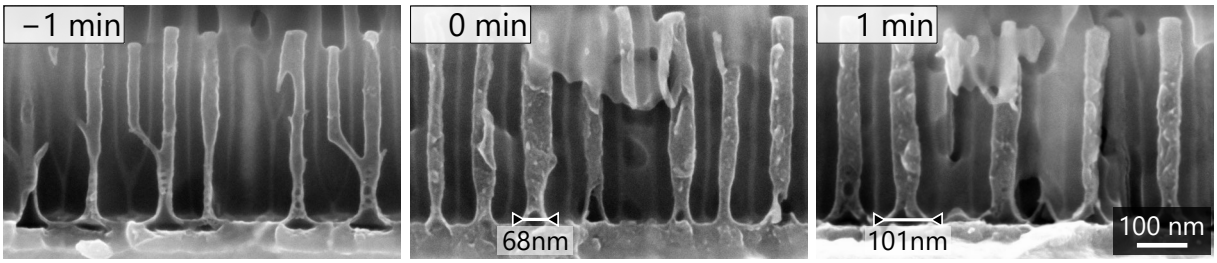

Figure 1.6: Cross-section SEM images of PAA-embedded nanocolumn arrays formed by PAA-assisted anodising of ¼Nb substrate with −1, 0, and 1 min substrate anodising followed by ≥5 V s^{-1} re-anodising ramp to 250 V.

These improvements were applied successfully to nitrogen-doped substrates (¼N, ⅕N) and even the titanium substrate without any additives. The most remarkable result was the formation of a stable (almost 100 %) column array formed from the Ti substrate re-anodised even up to 300 V. This demonstrates a considerable leap from published reports [10, 11], being able to achieve less than 20 % stability for re-anodising potentials over 60 V.

Breakdown

Here, the breakdown (BD) phenomenon refers to an event when the film is macroscopically destroyed during the anodisation, usually the re-anodising ramp. This event is usually associated with an abrupt increase in the current density. Therefore, the breakdown phenomenon indirectly limits the maximum anodising potential and thus the achievable length of the columns.

BD process can be influenced by the slope of the re-anodising ramp, as shown in Figure 1.7. For steeper ramps, the breakdown is characterized by a development of micro-arc anodisation (plasma electrolytic oxidation) that leads to a formation of micro-arc anodic oxide (MAO) [14, 15], shown in Figure 1.7:C1. On the other hand, during the slower ramp, the breakdown is accompanied by the delamination of a PAA-embedded a-MO_x layer from the metallic substrate in the form of circles, shown in Figure 1.7:C2. This delamination is believed to be caused by O_2 evolution and trapping below the a-MO_x layer. While the micro-arc anodisation breakdown gives a higher BD potential (330 V), usually much lower BD potentials can be achieved when a delamination BD occurs. In both cases, the breakdown develops within a small area and spreads with time over the whole surface of the sample.

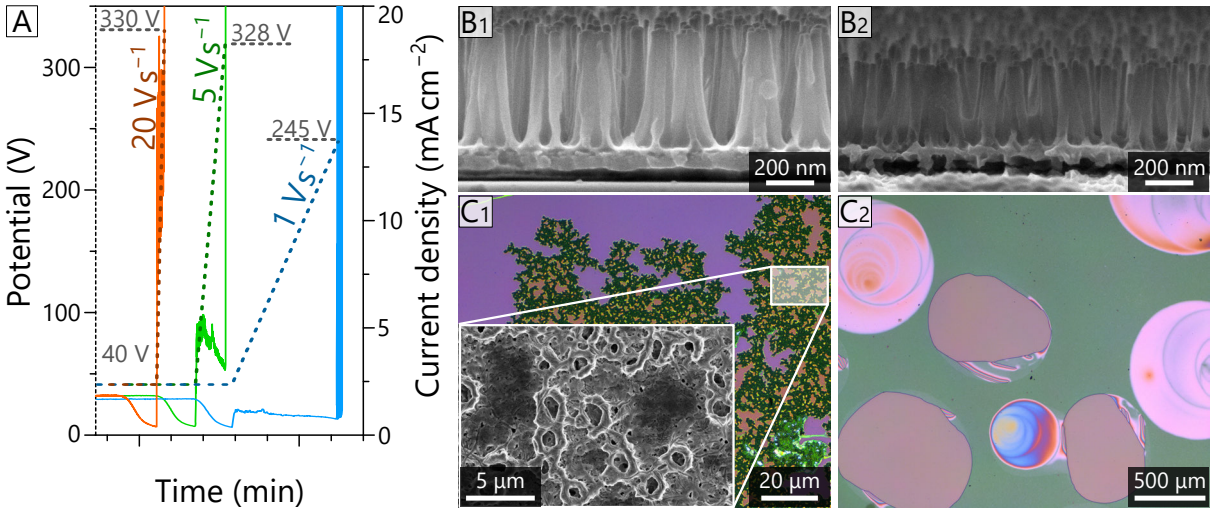

Figure 1.7: (A) Anodising curves for ¼Nb layer anodised in 0.3 M oxalic acid at 7 °C with 1 min substrate anodising period followed by a re-anodising ramp of 1, 5, and 20 V s^{-1}. (B) SEM cross-view images of the resulting nanocolumn arrays for (B1) 5 or 20 V s^{-1} and (B2) 1 V s^{-1} re-anodising ramp. (C) Optical images of the resulting features damaged by the breakdown process: (C1) micro-arc anodic oxide, (C2) film delamination in the form of bubbles caused by O_2 gas evolution and trapping at the interface.

The breakdown process does not influence the column morphology except limiting the maximum length and damaging the related area. On the contrary, it is assumed that the column morphology is the decisive parameter for the BD process since both depend on the start of the re-anodising and the re-anodising ramp sweep.

1.3.3 Electrochemical characterizations

In this part of the thesis, electrochemical characterization of PAA-embedded samples was done by cyclic voltammetry (CV), electrochemical impedance spectroscopy (EIS), and Mott–Schottky (M–S) analysis. In this case, the purpose of the CV is to demonstrate the electrochemical stability given by an aversion of the sample towards redox reactions. The EIS and M–S analyses were used to characterize and quantify the electrical properties of the system.

Based on the cyclic voltammograms (Figure 1.8) and voltage-dependent EIS (Figure 1.9), a rough insight into the electrochemical properties of the samples was obtained. Both the annealing treatment and the nitrogen doping of the initial substrate affect the measured donor density of the samples together with their conductivity. These findings can be categorized into two topics: the influence of the substrate and the post-anodising treatment.

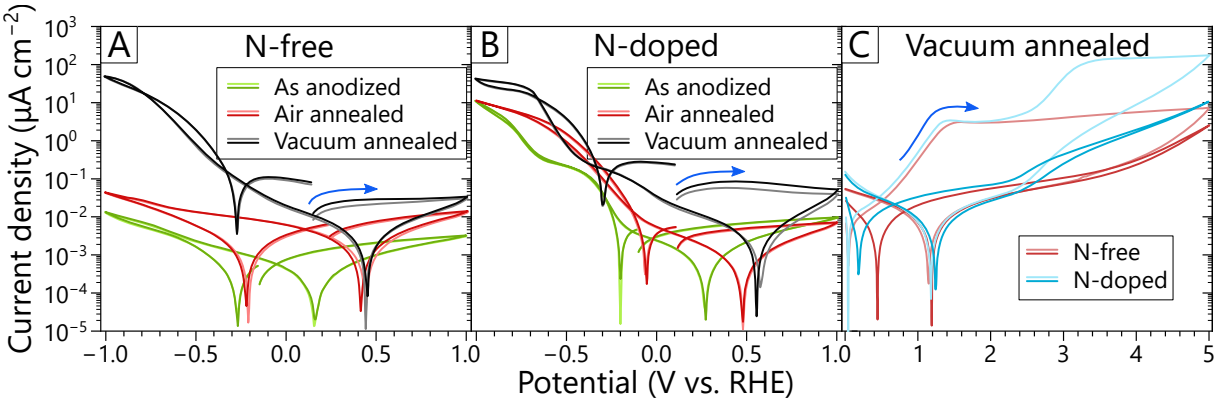

Figure 1.8: Cyclic voltammograms for as-anodized, air- and vacuum-annealed (A) N-free and (B) N-doped TiO_2 nanocolumn arrays. (C) Cyclic voltammograms of the vacuum-annealed N-free and N-doped arrays obtained at higher anodic potentials. A pale colour shows the first measured cycle of each sample, and blue arrows mark the scan direction. The current density is in absolute value and log scale.

The presence of nitrogen in the substrate layer increases the measured donor density and conductivity for all annealing treatments. N-doping is known to narrow the bandgap of TiO_2 or form impurity states, leading to enhanced light absorption.[16, 17] M–S analysis (Figure 1.10) of the N-doped arrays performed in this work shows a distinct plateau (Figure 1.10:B), which may be attributed to Fermi level pinning due to surface/trap states.[18] This may be an indication of the prevailing N-doping mechanism. Additionally, the CV of the vacuum-annealed N-doped samples shows a characteristic behaviour for TiN anodising that may hold some information about the presence of nitrogen in the columns.[19]

To summarize, the electrochemical properties of N-free and N-doped TiO_2 nanocolumns prepared by using PAA-assisted anodising, and post-anodising annealing in different atmo-

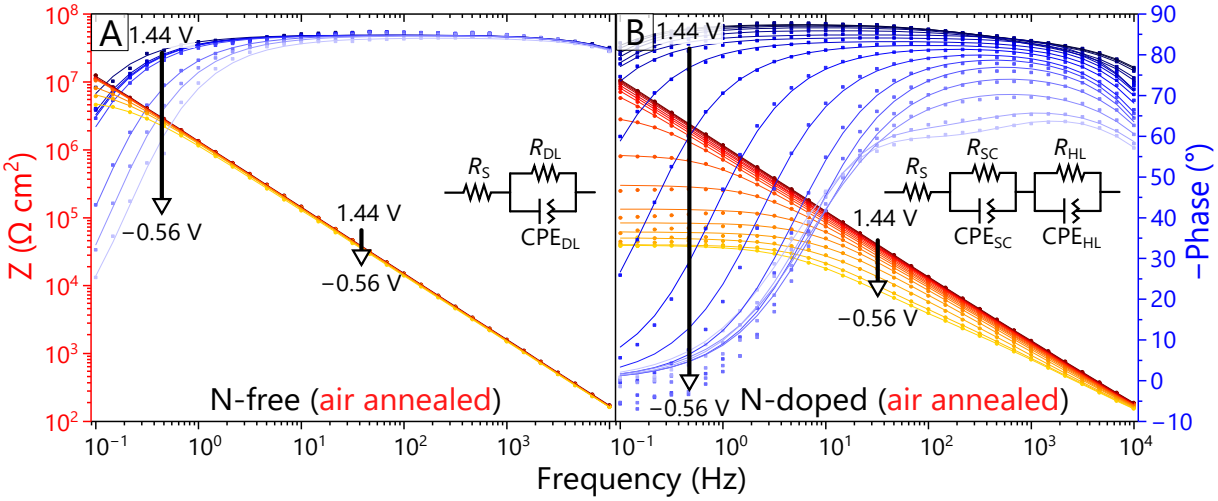

Figure 1.9: Bode plot representation of EIS measurements of the (A) N-free and (B) N-doped air-annealed nanoarrays obtained in the borate buffer at DC voltages from 1.44 to −0.56 V vs RHE. The measured data are represented by dots, whereas the solid lines are fitted equivalent electrical circuits shown as insets (SC = space charge layer, HL = Helmholtz layer, DL = dielectric layer).

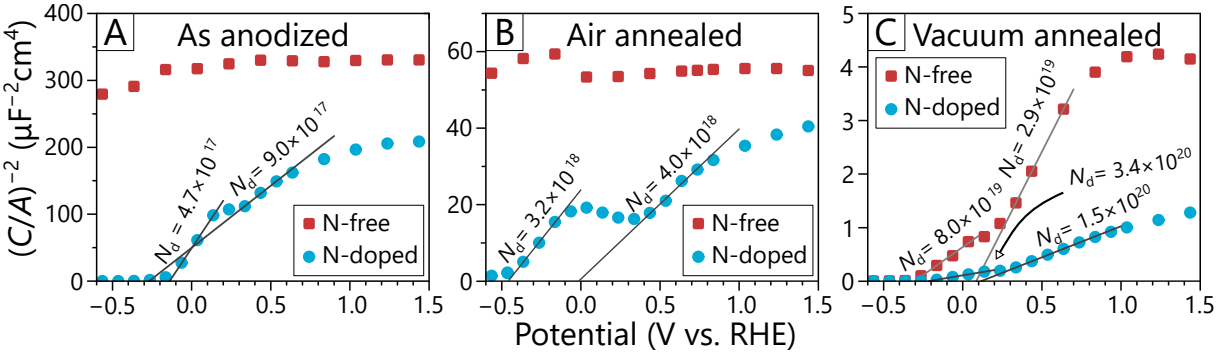

Figure 1.10: Mott–Schottky plots calculated from fits of the potential-dependent EIS measurements. The donor density (N_d) is given per cm^3.

spheres have been studied. Cyclic voltammetry and Mott–Schottky analysis has revealed that the incorporation of nitrogen and annealing in oxygen-deficient conditions lead to a significant rise of n-type donor concentration in the titanium-oxide-based nanocolumns. This demonstrates that the donor density, as well as the space charge layer of the columns, can be easily adjusted by these treatments.

The present findings are of vast importance for future utilization of the TiO_2-based nanocolumn arrays for photoelectrochemical water splitting to obtain nanocolumns with good electrical conductivity and a space charge layer localized at the column surface. Improving these properties will substantially enhance the photogenerated charge carrier separation in these nanoarrays.

1.3.4 Photoelectrochemical characterizations

Sample fabrication

Samples studied in this subsection are exclusively made from nitrogen-doped substrate layers, specifically ⅕N, ⅓N, and ¹⁄₁N (see Table 1.1). Samples were anodised in the large-scale setup with parameters chosen to match the previous study.[11] For the complete fabrication procedure, please refer to subsubsection 1.3.1. Afterwards, the surrounding PAA was partially (PE) or fully (FE) etched away (Figure 1.4) as described in subsubsection 1.3.1. The complete removal of PAA was applied only to the ¹⁄₁N nanocolumn layer (Figure 1.4:C2) as it is the only one that forms a fully stable nanocolumn layer for the given anodising conditions. Because the PAA etching may lead to a partial exposure of the metallic substrate (or aluminium residues), all samples were subsequently anodised one more time to a lower potential of 6 V to oxidize this layer. Samples were broken into smaller strips according to laser pre-engraved grooves (10 mm×20 mm).

Similarly to the samples prepared for the electrochemical investigations (subsection 1.3.3), part of the samples was annealed at 500 °C for 2 hours in the ambient atmosphere (AA), a vacuum (VA), or a hydrogen atmosphere (HA). Overall, 16 different samples were characterized, divided into two morphologies (with and without PAA, i.e., partially and fully etched, respectively), three substrates, and four different post-processing techniques. This series allows us to study the effect of nitrogen concentration within the substrate layer and study the effect of oxidizing or reducing thermal treatment. Lastly, in the case of the ¹⁄₁N substrate, the influence of the surrounding PAA can be discussed when the PE sample is compared with the fully exposed nanocolumns.

Additionally to the nanostructured layers, flat titanium oxide layers were prepared by thermal and anodic oxidation. A titanium sheet (1.5 mm thick) of high purity (99.999 %) was used as the starting material. The sheet was cut into 10 mm×30 mm strips, which were mechanically polished to a mirror-like finish. One sample was thermally oxidized in an ambient atmosphere for 5 hours at 550 °C. Other samples were potentiostatically anodised in 1 M H_2SO_4 aqueous solution at room temperature at 10 and 20 V for 15 minutes without any further annealing. The 10 V anodised sample gives a gold look (20 nm) while the 20 V anodised and air-annealed samples have a blue tint (50–70 nm).[20, 21]

Chopper light linear sweep voltammetry

Figure 1.11 shows the current density vs potential curves under chopped illumination of the 365 nm LED using the PE-SDCM setup for all samples. The photocurrent density (J_{ph}) can be easily extracted as the difference between the total current (J_{total}) and the dark current (J_{dark}), as illustrated in Figure 1.11:C. The photocurrent density of all samples increases with the anodic potential, which indicates the standard n-type nature of the electrode material. This growth is in good agreement with expectations and the previous M–S analysis (see subsection 1.3.3).

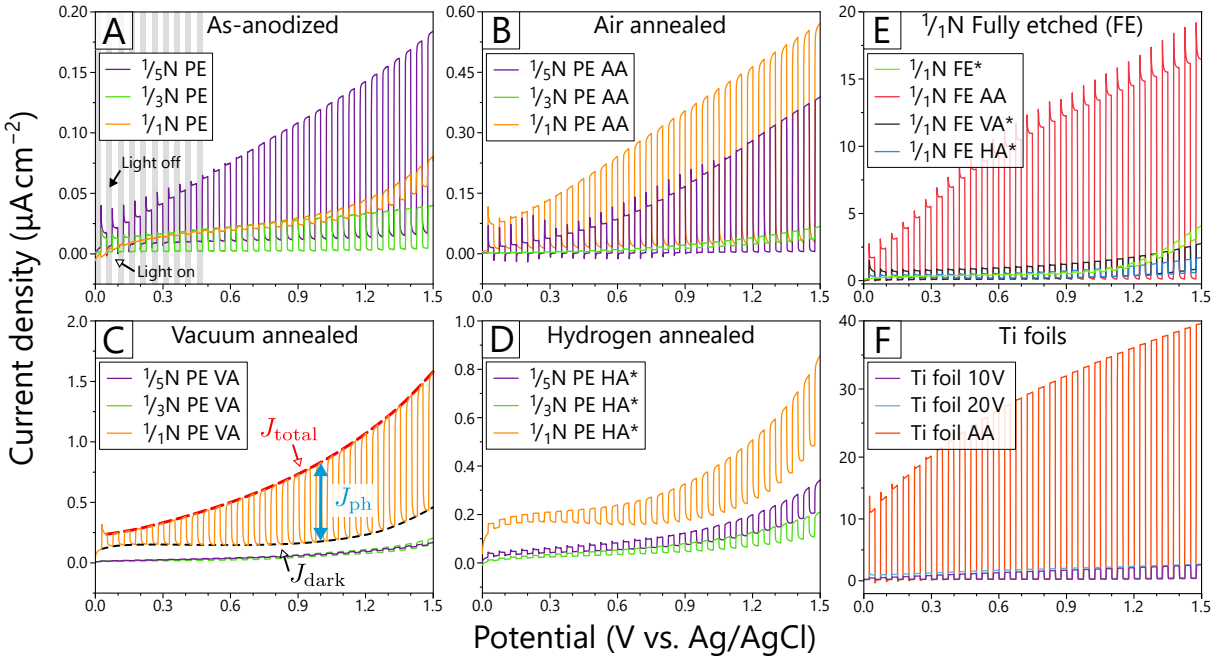

Figure 1.11: Photoelectrochemical properties of (A–E) nanostructured layers formed on nitrogen-doped substrates (Table 1.1) and (F) oxidized titanium foils. The chopped J–V curves were obtained under the 365 nm LED and illumination cycle of 5 s (frequency 0.2 Hz and cycle duty of 50 %, illustrated in (A)). Measurements were performed using the PE-SDCM in 0.1 M phosphate buffer and a scan rate of 10 mV s^{-1}. Samples marked by an asterisk (*) have been anodised to 4 V versus Ag/AgCl before measurement (as discussed in the following text).

IPCE measurements

Figure 1.12 presents a summarized comparison of IPCE obtained by PE-SDCM under 365 nm LED illumination for the various nanocolumn layers and compact oxide layers formed on a titanium sheet (used as a reference). These IPCE values were calculated from the photocurrents measured at 1 V versus Ag/AgCl. Several important trends can be observed here. The most significant outcome is that the highest IPCE of almost 3 % has been found for the thermally oxidized Ti sheet used as the reference. This value matches the reported values between 2–3 % for thermally oxidized Ti foils at 500–700 °C for 10–60 min.[22] The second-highest IPCE with a value of less than half of the AA Ti sheet was obtained for the PAA-free air-annealed layer (1/1N FE AA). The two anodic layers (10 V and 20 V) on the Ti sheet and the PAA-free vacuum-annealed layers (1/1N FE VA) are in the middle, close to but still over the 0.1 % level of the second-highest IPCE. The rest of the MO_x nanostructured layers are left far behind with relatively poor performance.

The observations mentioned above indicate that, in the case of the studied TiO_2-based nanocolumns, the planar MO_x layer grown below the nanocolumns has a crucial impact on the IPCE values and the a-MO_x nanocolumns do not bring a significant improvement.

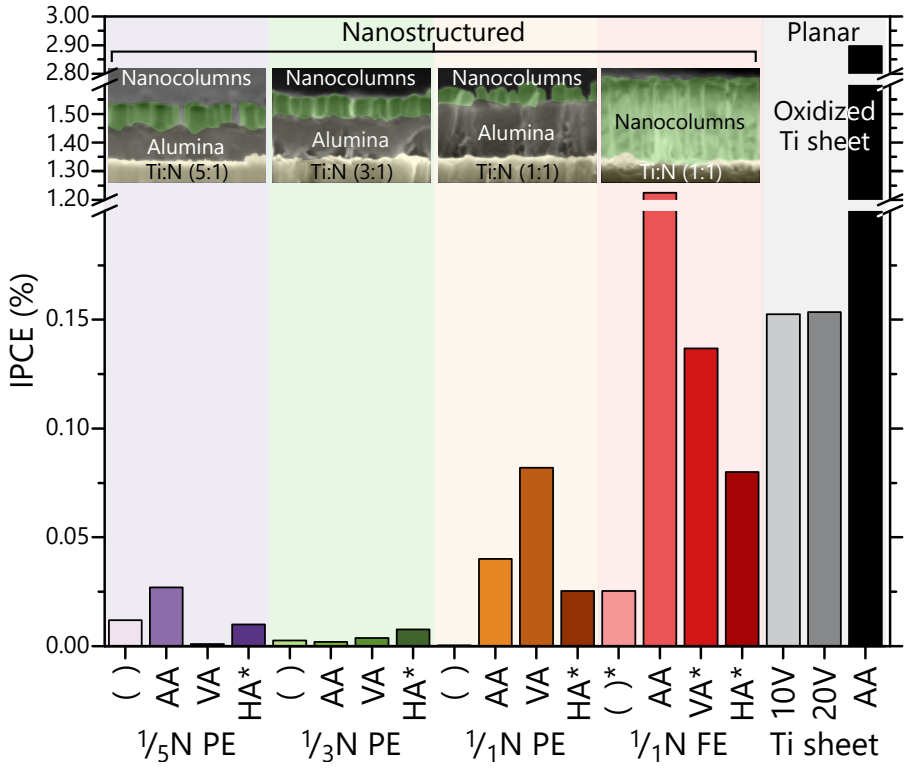

Figure 1.12: A comparison of the IPCE values measured in the PE-SDCM setup under the 365 nm LED illumination (3.4 eV) at the applied bias of 1 V versus Ag/AgCl (the corresponding voltammograms are shown in Figure 1.11). The labels are consistent with the fabrication section (subsection 1.3.1): partly etched (PE), fully etched (FE), as-anodised ( ), and annealed in the air (AA), vacuum (VA), or hydrogen (HA) atmosphere. Two layers formed by anodic oxidation of the Ti sheet in a sulphuric acid electrolyte are added, marked by their anodising potentials: 10 V and 20 V. Insets show false colour SEM cross views of the nanostructured layers (green – nanocolumns, grey – alumina, yellow – substrate). High-resolution SEM images of and further information about the nanocolumn samples are shown in Figure 1.4.

This hypothesis is confirmed by the following conclusions:

(i) The IPCE of the 1/1N FE AA sample is over 20× higher than that of the same film but PE, even though the difference in the active area (the surface of the columns and the substrate) is only up to 4× larger. Therefore, this extensive increase must be attributed to the layer of thermal oxide grown on the substrate during air annealing.

(ii) The structure of the formed nanocolumns contains voids (hollow parts). In the case of 1/5N and 1/3N layers, usually, a singular void is located under the root. In contrast, the 1/1N columns form a predominantly hollow structure. Unfortunately, the hollow profile is assumed to be less advantageous to the solid column due to low light absorption, electrical conductivity, and charge separation.

(iii) The performance of the 1/1N FE AA layer with or without nanocolumns is almost identical, as shown in Figure 1.13:D. The observed difference in the lower wavelengths is presumably caused by the nanocolumn residues after their removal by a

cloth cleaning swab stick (Figure 1.13:C). Therefore, the contribution of nanocolumns to the IPCE is either negligible or zero.

(iv) Among the PE series, just the ⅕N gives the highest IPCE values for the AA layer. The reason is that the ⅕N PE samples suffer from the largest exposure of the underlying substrate caused by alumina defects (discussed in subsubsection 1.3.1). The subsequent air annealing leads to its additional oxidation and formation of a localized thermal oxide film that probably carries most IPCE. This effect is analogous to the ¹⁄₁N FE AA but much weaker due to a partial exposure of the substrate.

(v) Like in the previous point, a correlation between the exposed substrate area and the IPCE value of the as-anodised samples can be observed in the increasing order from ¹⁄₁N PE < ⅓N PE < ⅕N PE < ¹⁄₁N FE. Same as in the case of air annealing, the exposed area is oxidized by the post-anodising process. However, the IPCE enhancement caused by the additional anodic oxide is much smaller compared to the thermal one. An analogy can be noted for anodised and thermally annealed Ti sheets.

(vi) Lastly, the thermally oxidized planar sample (Figure 1.13:A) has approximately 2× higher performance than the nanocolumn version (Figure 1.13:B), as illustrated on the ¹⁄₁N substrate shown in Figure 1.13:D. This difference suggests that nanocolumns not only have a poor additional value to the IPCE of the system (as discussed in point iii)) but also somehow hinder the possible performance of the thermal oxide. This shadowing can be roughly supported by the geometry of the system, where the nanocolumns take up to 25 % of the 2D projection, and the root takes an additional 30–35 % of the oxide surface, giving together approximately 50 % of the missing performance. Even though the poor performance of nanocolumns was indirectly proven, the similar behaviour of the root area is just a speculation, as it is not possible to separate it from the substrate oxide.

Furthermore, the performance of the as-anodised layers is, in most cases, notably low. It can be seen for the ⅓N, ¹⁄₁N substrates, and especially for the anodised titanium sheet (Figure 1.12). Although the air annealing of the Ti sheet and its anodising at 20 V produces oxide films of similar thickness (50–70 nm; estimated from the colour and literature)[20], their performances are apart by order of magnitude. This performance gap originates from the different crystal structure of the oxide formed by the anodisation (amorphous), and the thermal oxidation (anatase or rutile), as will be discussed in later texts. This difference between as-anodised and air-annealed oxides also supports point v).

Point vi) assumes the equivalence between MO_x layers formed on the planar substrate with the 185 nm thickness (Figure 1.13:A) and the one formed through the nanocolumn layer (Figure 1.13:B, C) with the thickness of 128 nm. Although these layers differ in their thickness, it is assumed that it does not play a significant role. The reason for neglecting this apparent difference is based on the IPCE comparison of a much thinner layer that performs better than the 128-nm layer. Therefore, the thickness cannot be a dominant

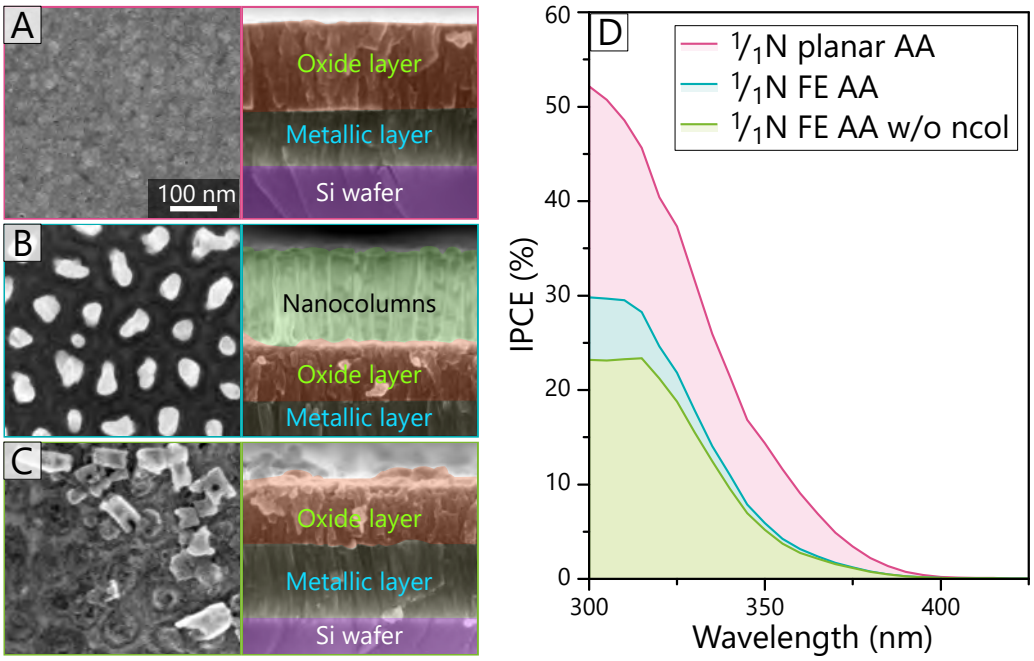

Figure 1.13: SEM top and cross-section views of (A) a compact MO_x layer (185 nm) formed by thermal oxidation (same as for the air-annealed nanostructured samples, 550 °C for 2 h in the ambient atmosphere) of the 1/1N substrate layer. Before annealing, the superimposed aluminium layer was removed by a 1 M NaOH aqueous solution. The 1/1N FE air-annealed nanocolumn array with 128 nm thick oxidized substrate layer (B) before and (C) after column removal. (D) IPCE spectra of these layers measured by the photoelectric spectrometer setup at the applied bias of 1.5 V versus Ag/AgCl.

cause for the 128-nm layer formed under nanocolumns to perform worse than the 185-nm layer formed over a free surface.

More surprising is that these oxide layers have an almost identical chemical composition with a zero nitrogen content, as estimated by XPS.These findings demonstrate that the thermally grown oxide has stoichiometry very close to a pure TiO_2. In all cases, the thermal TiO_2 layers should be composed of the anatase phase, according to numerous reports.[21–24] These annealing parameters (550 °C for 2 h in the ambient atmosphere) were chosen as they were reported to give the highest ratio of anatase phase, which results in large photocurrents and IPCE values.[24, 25] A higher temperature treatment leads to the formation of the rutile phase, which has a lower bang gap (3.0 eV) than anatase (3.2 eV) but, in general, gives a worse photocatalytic activity.[24]

Conclusions

This section investigates the photoelectrochemical properties of the selected nanocolumn layers formed by PAA-assisted anodising of titanium substrates of various nitrogen contents. Here, the anodising parameters were chosen to obtain the same column morphol-

ogy as studied in our previous work.[11] Unfortunately, using these parameters (a long substrate anodising with the slow re-anodising ramp) resulted in very unstable columns (subsection 1.3.2), except for the ¹⁄₁N substrate. Therefore, the PAA has to be only partially removed to reveal only the tops of the columns while still leaving a sufficient layer for their support.

Although this solved one problem and allowed us to compare the effect of various nitrogen concentrations in the substrate for nanocolumn layers, it also has created a new problem caused by the inhomogeneous etching of the PAA. This process revealed the underlying substrate layer to varying degrees depending on the thickness of the partly etched PAA layer related to the substrate composition (column length). Therefore, the layers were anodised (post-anodising) after etching to oxidize all metallic surfaces accessible to the electrolyte. Furthermore, the samples were thermally annealed in various oxidizing or reducing atmospheres to study the effect of the created oxygen vacancies. The presence of the supporting PAA layer creates an additional issue because it is incompatible with common and well-performing electrolytes used for photoelectrochemical characterization of TiO_2, such as $NaSO_4$ or NaOH. To avoid the undesirable etching of the PAA, phosphate buffer was chosen for all experiments.

Based on all findings, the most significant conclusion is that the prepared nanocolumns have negligible IPCE performance and thus are not feasible as a photoelectrode material. The most convincing argument is the IPCE comparison between a nanocolumn layer before and after columns being wiped, showing a minor difference. Even though, this decrease cannot be unambiguously associate only with the removal of nanocolumns. A more reasonable explanation can be simple shadowing of the surrounding more active thermal oxide by nanocolumn residues. This outcome is even more highlighted when the nanostructured surfaces show just a fraction of performance compared to the flat oxide layers, which are considerably less demanding in terms of the fabrication requirements.

This poor performance is assumed to be primarily related to the morphology of the selected nanocolumns. The formed nanocolumns consist of defects in the form of voids located near the root for substrates of lower nitrogen concentrations (¹⁄₅N, ¹⁄₃N), while for the highest nitrogen concentration (¹⁄₁N), the nanocolumns have the characteristic hollow structure. The voids are surrounded by a very thin TiO_2-based shell, presumably not a great electrical conductor, light absorber, or electron–hole separator.

The chemical composition is another factor that can play a significant role. This can especially be related to the less stable nanocolumns (¹⁄₅N, ¹⁄₃N), in which the roots consist of a mixture of titanium and aluminium oxides that makes them chemically unstable and less conductive.

1.4 Conclusions and future outlook

This part of the thesis studied the morphology and electrochemical and photoelectrochemical properties of titanium oxide nanocolumn arrays formed by the porous anodic alumina-assisted anodising of a superimposed aluminium layer over titanium-based substrates. The general goal of this work was to fabricate and analyse nanostructured TiO_2-based layers, which could possibly be used as a photoanode for photoelectrochemical water splitting, otherwise termed as the production of solar hydrogen.

The fabrication section demonstrates two anodising setups successfully used to prepare a variety of samples:

1. The flow-through pressing cell that can be used with significant advantages in R&D applications where a broad variability of anodising parameters is required.
2. The large-scale setup that can be, on the other hand, utilized for applications requiring large sample areas and homogeneous processing.

The etching of PAA was optimized to achieve the same exposure for various heights of the nanocolumn arrays. However, it was found that it leads to the formation of defective sites, which have a crucial impact on further evaluating PEC properties of partly etched samples.

The electrochemical characterization of the PAA embedded nanocolumns (subsection 1.3.3) confirmed most of the expectations. A significant difference between the behaviour of the layers formed on pure (N-free) and nitrogen-enriched (N-doped) titanium substrates was identified. The N-free nanocolumns showed classical dielectric properties for the as-prepared and air-annealed samples, while the N-doped layers gave a desirable (n-type) semiconducting behaviour for all post-processing conditions as confirmed by Mott–Schottky analysis. It was also revealed that the selected parameters of the vacuum annealing treatment lead to a substantial increase in the dopant concentration, presumably in the form of oxygen vacancies. These findings agree with the literature. Even though these results did not deliver any significant novelty to the field, they are of vast importance for future utilization of the TiO_2-based nanocolumn arrays for photoelectrochemical water splitting. They describe how to obtain nanocolumns with good electrical conductivity and a space charge layer localized at the column surface and how to enhance the photogenerated charge carrier separation in these nanoarrays substantially.

The photoelectrochemical properties of nanocolumn layers (subsection 1.3.4) were investigated during an internship at JKU in Austria. For this purpose, a custom-built illumination system was constructed and added to the experimental PE-SDCM setup. Additionally, the results obtained by this setup were validated by IPCE measurements performed on a photoelectric spectrometer by Dr Miloš Krbal (University of Pardubice). In summary, the prepared nanocolumn layers showed only minor photoelectrochemical performance based on the IPCE results. The nanostructured layers were greatly overperformed by flat thermal or anodic oxides formed by technologically more straightforward

methods. The reason is probably the characteristic hollow morphology of the nanocolumns formed by the chosen substrate composition and anodising parameters. This influences not only the morphology of the nanocolumns but also their chemical stability to withstand the PAA etching. Due to this reason, the comparison between the nanocolumns formed on substrates of different nitrogen contents could be performed only between arrays still partly embedded in the alumina layer.

This issue was later addressed by a systematic study of the effect of anodising conditions on the morphology and stability of the formed nanocolumns (subsection 1.3.2). The most critical outcome demonstrates the possibility to fabricate a perfectly stable nanocolumn array re-anodised to up to 300 V even from the pure Ti substrate. This is an overwhelming advancement compared to the previous reports on achieving stable arrays only to re-anodised potential up to 40 V. Besides the increase of stability, the improved anodising conditions also lead to a more compact/solid column structure without undesirable voids.

Unfortunately, further photoelectrochemical investigation of these novel layers was not conducted within the time scope of this thesis. However, the current findings present solid foundations for a future comprehensive study comparing both effects of the substrate composition and the nanocolumn morphology. All of this without any complications with the stability of the nanocolumns, and thus wholly avoiding the supporting alumina layer. Therefore, it is believed that these improved nanocolumn layers may provide a much higher IPCE when compared to the ones presented in this work. On the other hand, it is questionable whether they can rival other materials in PEC water splitting, where other methods can easily achieve a larger surface area and higher light absorption. The objective reason for this is that the PAA-assisted anodisation cannot deliver the same flexibility in the prepared structures hand in hand with a simple fabrication process. On the other hand, currently, there is no utilization of the nanostructured prepared by PAA and the ability to achieve a high order for the PEC. Therefore, it is advised that future studies also focus on the unique advantage of this technique that can be utilized in optical sensing.

2 TEMPLATE-BASED FABRICATION OF GOLD NANOPARTICLES

Plasmonics on metal nanoparticles has been extensively investigated for its wide application area in, e.g., optical sensing, light generation, biomedicine, electronics, and data storage.[26] Among other plasmonic NP candidates (Ag, Cu) having their LSPR in the visible region, AuNPs are preferred especially for biological applications due to their inert nature and biocompatibility,[26] and easy functionalization provided by the thiol-gold association.[27] The increased utilization of AuNPs in recent decades quickly reflects the growing demand for their application-tailored production.

This part of the thesis demonstrates one of the AuNPs fabrication methods. AuNPs are synthesized by a solid-state dewetting (SSD) of a thin gold film deposited on nanobowled aluminium (Al) templates. The Al templates are prepared by controlled anodic oxidation of the Al sheet and subsequent removal of the formed porous anodic alumina (PAA). Thus, similarly to the previous part, this fabrication technique utilizes the PAA morphology that forms the bottom Al template. In contrast to the PAA-assisted anodisation (section 1.2), this time, the focus is on the self-ordering phenomenon of the PAA, resulting in an almost uniform hexagonal alignment. This way, it is possible to prepare a 2D array of highly ordered AuNPs with tunable properties, e.g., size and spacing. This AuNP array was further transferred to various transparent substrates to obtain the LSPR element.

This work was conducted in close collaboration with Dr Attila Bonyár (Department of Electronics Technology at Budapest University of Technology and Economics, Hungary), who demonstrated a label-free DNA biosensing on these AuNP layers. This real application proved that these plasmonic nanostructures could be used as a versatile optical sensing platform (illustrated in Figure 2.1) for the detection of a large variety of receptor–target molecular interactions (e.g. nucleotide sensors or immunosensors). This biosensing part can be found already in the published joint study [28].

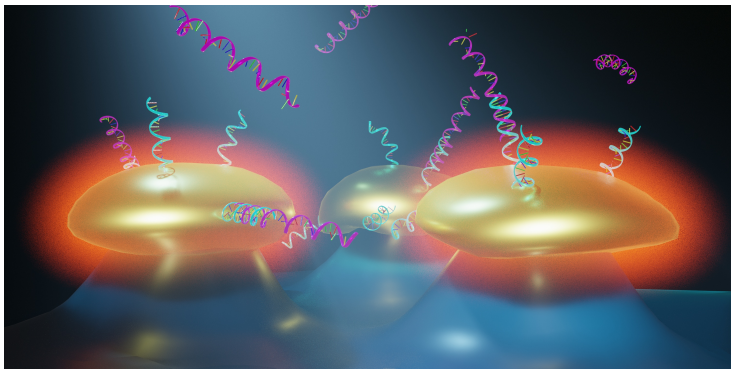

Figure 2.1: Graphical illustration of mushroom-like plasmonic structures functionalized by single-stranded DNA (ssDNA) probes (cyan) for the detection of target ssDNA (magenta).

2.1 Motivation and aims of the work

In recent decades, a phenomenon called localized surface plasmon resonance (LSPR) on metal nanoparticles has attracted much attention due to its many favourable properties such as the high sensitivity of resonance conditions to the dielectric properties of the ambient medium; confinement of light within a nanometer region, or a large electromagnetic field enhancement around the particles. Nowadays, LSPR flourishes above all in optical sensing, where it pushes the boundaries of the sensitivity of molecular detection. It has naturally created a vast demand for application-tailored and affordable plasmonic nanostructures.

The fabrication method proposed in this work (illustrated in Figure 2.2) is based on the controlled, template-assisted SSD synthesis of AuNPs and their transfer to a transparent substrate. The motivation for this work is the technology has distinct advantages in comparison to other methods, such as:

(i) Controlled synthesis: the particle size and interparticle distance can be well controlled in a sub-100 nm hexagonal distribution, and thus the plasmonic absorption peak (and sensitivity) in VIS range can be fine-tuned for individual applications. Besides plasmonic sensing, the absorption peak should be tuned for surface-enhanced Raman scattering (SERS) applications as well, where the relation between the resonance peak of the substrate and the excitation wavelength defined by the laser affects the SERS enhancement.[29, 30]

(ii) Large-scale fabrication: the lateral size of the substrate is not limited, sensors with several cm^2 surface area can be easily prepared, and the nanoparticle size/distribution is homogenous on the whole surface. Such large sensor areas are required for LSPR imaging (LSPRi) applications [31] and beneficial for SERS.[32, 33]

(iii) Robustness: the prepared nanocomposite—gold nanoparticle arrangement fixed on substrate pillars—is stable to a great extent; no particle removal exposed to fluidic environments. The surface of the gold can be cleaned multiple times with low-power O_2 plasma without any significant drop in sensitivity.

Like many other inventions, this fabrication technique has been discovered a way before it found its application. The origin dates to 2014, when this concept—AuNPs fabrication by utilizing well-ordered nanobowled aluminium as a substrate for template-assisted SSD of the thin gold film—was published in the author's master thesis [34]. To our knowledge, this is the first report of this technique.

A similar method was published in 2011 by Yang et al.[35], where they used a self-organized monolayer colloidal crystal (MCC) composed of polystyrene spheres (diameter of 0.5, 1 and 2 µm) to form a bowled template for SSD of the thin metal film. One of the first attempts utilizing the self-ordered PAA for SSD of gold film and pushing AuNP diameter into sub-100 nm range were in 2013 by Yingwei et al.[36] and in 2014 by Jo et al.[37] In both cases, the authors used PAA with broader pores as the template for SSD.

Compared to the inconclusive results of Yingwei et al., Jo et al. show a high-quality work focusing on SERS application. Similarly, in 2016, Altomare, Nguyen and Schmuki [38] used SSD of various Au/Ag layers on TiO_2 nanotube arrays showing improvement in their photocatalytic activity.

In the same year (2016), a part of this work was published in a conference proceeding. [39] Here, the fabrication method was extended by the AuNP size control and, for the first time was demonstrate the sensing properties of this AuNP array thanks to its transfer from Al template to simple polydimethylsiloxane (PDMS) microfluidic cell. Later, in 2017 Fan et al.[40] and in 2019, Ikeda et al.[41] published their results of AuNPs formed by the same technique. In both cases, they focused only on the fabrication method, showing the effect of template dimensions, the thickness of the deposited layer, or annealing parameters. Even though these works conducted a very similar study, there are a few deviations in the results, which will be in more detail discussed in the experimental section 2.2. In the most recent work published in 2020 [28], we show a comprehensive fabrication method of AuNP layers, their transfer on the epoxy substrate, and utilization for label-free DNA detection.

This work aims to demonstrate the fabrication of the AuNP array as a feasible LSPR sensor. Through the development process of this technique, many issues have been overcome, which may represent individual objectives:

1. Achieve a high uniformity in the distribution and alignment of AuNPs within the array.
2. Develop a method to control the dimensions of AuNP arrays, especially the diameter and spacing of the AuNPs.
3. Utilized the AuNP array as an LSPR-based sensor, and thus its transfer to an appropriate transparent substrate.
4. The final micromachining of the nanocomposite to enhance its performance.

2.2 Experimental, results & discussion

This experimental section is structured according to the scheme shown in Figure 2.2, where the fabrication method is divided into three thematic parts: fabrication of nanobowled aluminium template (processes 1–3), furthermore split into the aluminium preparation and formation of self-ordered PAA; formation of AuNPs on the template by solid-state dewetting of a gold thin-film (processes 3–5); and transfer of AuNP layer to another substrate, its modifications (process 5–8) and characterization of prepared nanocomposite material.

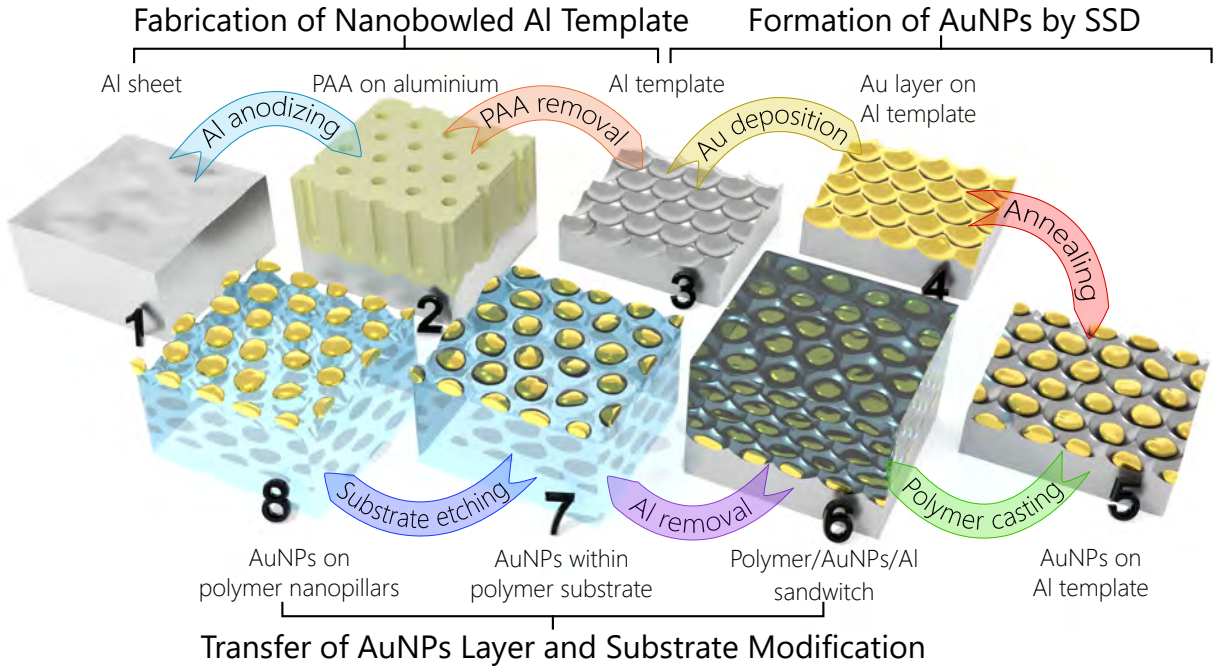

Figure 2.2: Comprehensive 3D illustration of the technology to fabricate ordered gold nanoparticle arrangements on transparent (polymer) substrates. The main steps of the process are the following: (1) Preparations (cleaning, annealing, mechanical and electrochemical polishing) of the aluminium sheet. (2) Formation of PAA on aluminium through controlled anodic oxidation. (3) PAA selective removal and the reveal of a nanobowl Al template. (4) Thin gold film deposition on the Al template. (5) Formation of AuNP layer by solid-state dewetting of the Au film. (6) Transparent substrate (polymer) casting and curing on top of the AuNP layer. (7) Removal of the Al sheet to reveal transferred AuNP layer on the transparent substrate. (8) Substrate etching to boost up the performance by enhancing the surface accessibility of AuNPs.

2.2.1 Aluminium preparation

Aluminium foil with high purity of 99.999 % was chosen as the starting material, temper: as rolled, with the size of 100 mm×100 mm and thickness of 250 µm from Goodfellow Ltd.Before cleaning, the aluminium foil was cut to 50 mm×25 mm samples, and any

bending was flattened by rolling. Samples were then ultra-sonicated in acetone, washed in isopropyl alcohol (IPA) and deionized water (MiliPore, 18.2 MΩ). To increase the aluminium grain size and relax materials, samples were annealed at 550 °C for 15 hours (heating ramp of 10 °C min^{-1} with natural cooling). Vacuum (pressure less than 10^{-4} Pa) annealing was performed to avoid thermal oxidation.After annealing, the samples were mechanically polished to decrease the surface roughness and create a mirror-like finish.

The last step of preparation was electrochemical polishing of the Al foil. Electrochemical polishing not only smoothed the surface , but it also removed a thin top layer that was mechanically deformed due to previous mechanical polishing.Samples were electropolished on one side in standard 1:4 (v:v) perchloric acid (70 %) and ethanol (99.8 %) solution. Before polishing, the whole backside and a corner strip at the front side (placed between the contact and immersed area, where the solution level is located) was covered by a low tack self-adhesion PVE tape. This protection film decreases the overall current requirements (current density can reach over 300 µA cm^{-2}) and avoids the air/solution/solid interface where polishing is dramatically accelerated. The electropolishing is performed in a simple two-electrode setup.

2.2.2 Formation of self-ordered nanobowled templates

Two well-known anodising approaches using anodising in sulphuric acid at 25 V and oxalic acid at 40 V, with anodising conditions tabulated in Table 2.1, were adopted for this work.

Table 2.1: anodisation parameters used for template fabrication.

anodising potential*	Electrolyte	Temperature	anodising time
25 V	0.3 M sulphuric acid	2 °C	18 h
40 V	0.3 M oxalic acid	5 °C	20–25 h

* Values are used as the notation for anodising processes and type of templates in the following text.

Aluminium foils (50 mm×25 mm) prepared by previous processing (annealing, polishing, and cleaning) were processed by one-step anodising performed potentiostatically in the same two-electrode setup used for electrochemical polishing. To avoid unnecessary consumption of Al, a masking was applied after 20 min of anodization.

After anodisation, the samples were washed in deionized water. The exposure of the nanobowled aluminium structure was done by selective removal of the formed PAA. This removal was done in a water solution of 0.42 M phosphoric acid (H_3PO_4) and 0.2 M chromium trioxide (CrO_3) at 65 °C for at least 2 h (based on the etching process from ref. [13]), followed by thorough washing and ultra-sonication in deionized water. The mixture of H_3PO_4 and CrO_3 effectively dissolved (≈10 nm min^{-1}) the anodic alumina (or native oxide), leaving the residual aluminium intact. The resulting nanobowled aluminium

structures (Figure 2.3) were subsequently used as a template for solid-state dewetting of the thin gold layer.

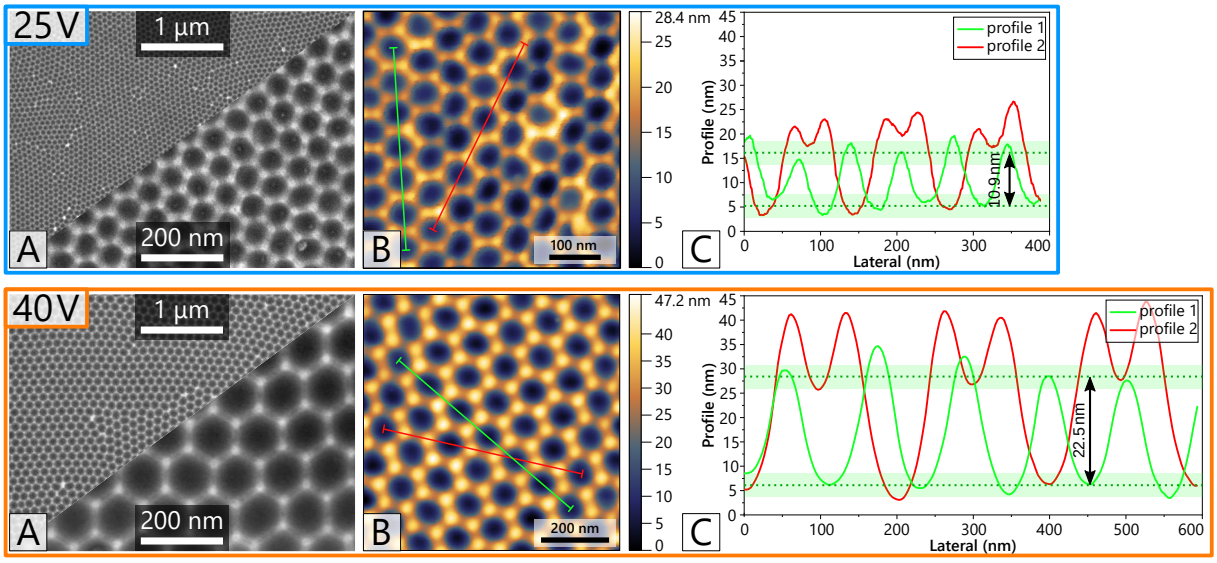

Figure 2.3: (A) SEM and (B) AFM images of Al templates prepared by 25 V and 40 V process. (C) The extracted profiles show the height of protrusions and the depth of nanobowls. Measured cell sizes are 65 ± 3 and 106 ± 4 nm for the 25 V and 40 V process, respectively.

2.2.3 AuNPs fabrication

The fabrication of gold nanoparticle (AuNP) layers by utilizing solid-state dewetting (SSD) of a thin gold film over the nanobowled aluminium templates is presented. When a gold-coated Al template undergoes thermal treatment, it produces a gold nanoparticle layer where the nanoparticle alignment is directly inherited from the Al template topography.

The experimental part is devoted to optimization the deposition and annealing parameters concerning SSD outcomes. All experimental work was performed with Al nanobowled templates of 25 V and 40 V types as a starting material (discussed in subsection 2.2.2).

Thin-film deposition techniques

The deposition of thin gold films was done by Physical Vapour Deposition (PVD) techniques, which use the vapour phase to deposit layers of atoms/molecules onto a solid substrate. Among other methods a magnetron sputtering using BESTEC Magnetron sputtering system showed the best properties (Table 2.2). The deposited rate was monitored before each deposition by QCM. Additionally, it was controlled by mechanical profilometry and XRR.

Deposited films have the smoothest morphology with fewer defects than film formed by an evaporation. Thus, it was possible to achieve AuNP layers of better quality, even for smaller 25 V templates.

Table 2.2: Deposition parameters of the evaporator setup. These deposition parameters were used for the samples prepared in the Evaporator setup, if not stated otherwise.

WD	α	r_s	P_{init}	P_{dep}	ω	R_{dep}
200 mm	29°	25.4 mm	10^{-6} Pa	10^{-1} Pa	10 RPM	3.5×10^{-2} nm s^{-1}

AuNPs controlled enlargement

AuNP size control is one of the main objectives of this work. As it directly influences the LSPR, it opens new possibilities for utilization in various applications (e.g., LSPR, SERS, SIERA). Naturally, the size of AuNPs depends on the amount of deposited material—Au film thickness. Unfortunately, it is restricted to a narrow window of values, as discussed in the previous subsection (subsubsection 2.2.3). To overcome this limitation, a repeated deposition and dewetting process were applied to increase the size of AuNPs (illustrated in the inset of Figure 2.4).[42, 43] It is important to point out that this process is still governed by the same principles as the first deposition and dewetting cycle when the best result can be achieved only in a narrow window of deposited film thicknesses. Figure 2.4 shows examples of various thicknesses of the deposited film for three cycles on 40 V templates. Again, not optimal thickness leads to poor template-assisted dewetting; NPs merging for too thick films and small satellite NPs for too thin films. The best outcomes, the main line, were achieved by 8 + 7 + 5.5 nm and 6 + 5 nm for 40 V and 25 V templates, respectively (shown in Figure 2.5). Since the thickness decreases with the cycle to retain a good NP separation, it becomes challenging to keep a compact film and avoiding undesirable splitting. These boundary conditions naturally limit the number of cycles to three and two for 40 V and 25 V templates, respectively.

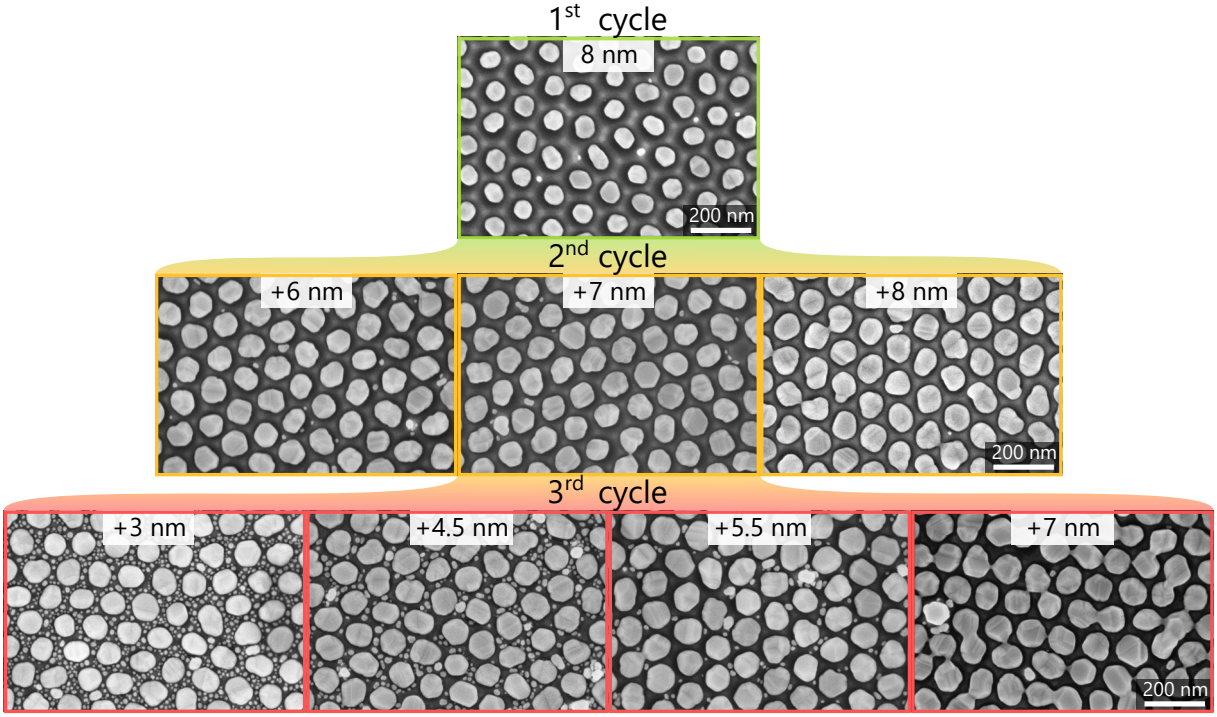

Figure 2.4: SEM images showing various cycle stages of repeated deposition and annealing over 40 V template with the schematic illustration of fabrication cycles.

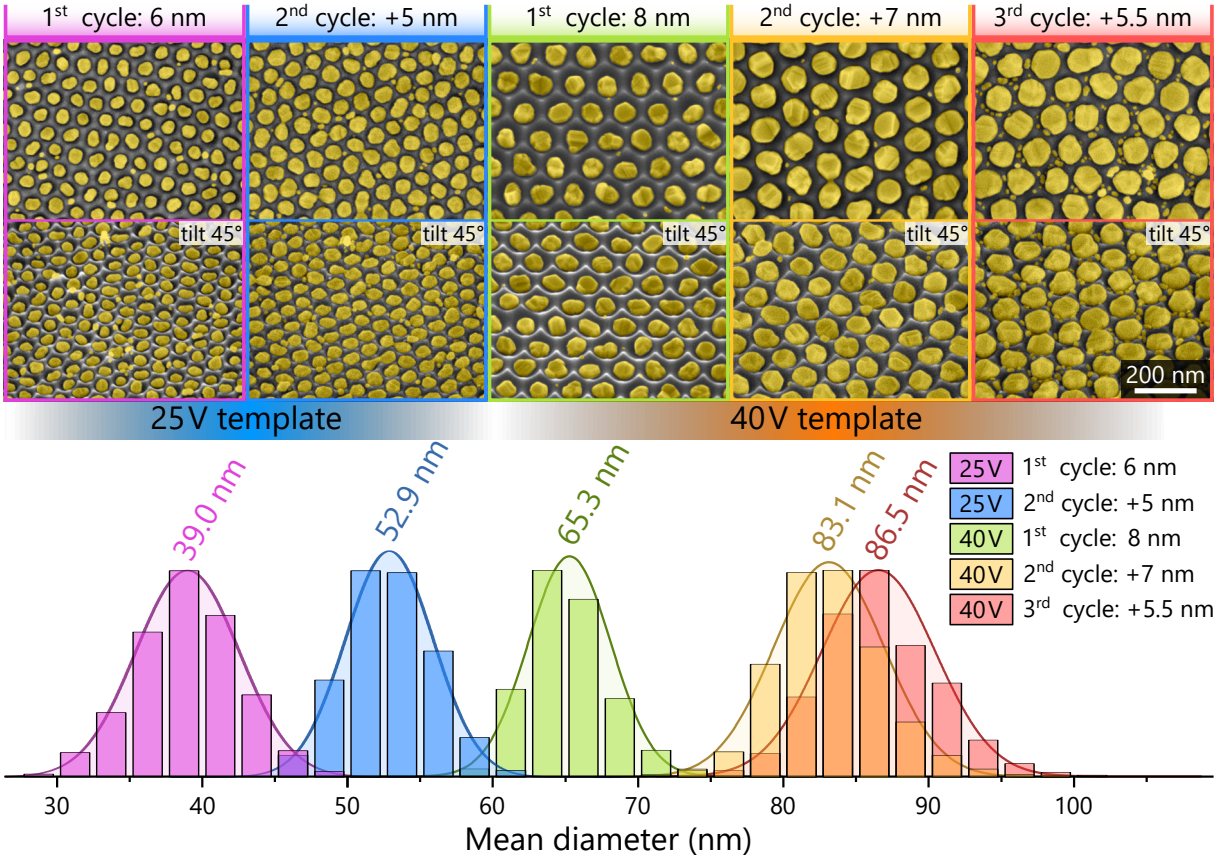

Figure 2.5: SEM images of the main lines of AuNPs formed over 25 V and 40 V Al templates with the corresponding size distribution (mean diameter) fitted by a Gaussian function. Mean diameters for 25 V are 39.0±1.8, 52.9±1.5 nm, and for 40 V are 65.3±1.4, 83.1±1.9, 86.5±2.0 nm.

2.2.4 Transfer of AuNPs layers

To utilize the fabricated AuNP layers as an LSPR sensor element, they were transferred to an electrically non-conductive and optically transparent substrate. During this process, a new substrate is cast over the AuNP layer, and the Al substrate is removed by chemical etching. The ideal substrate should be optically transparent in the region of plasmon resonance (VIS) with low diffusion. Additionally, it has to be compatible with fabrication processes, including good chemical stability to acids, bases, and organic solvents and has sufficient thermal stability to withstand wet or dry etching processes. Other critical property such as good adhesion to AuNPs, durability, and cleanability will also be evaluated.

In the course of this work, four main types of substrate materials were tested: polydimethylsiloxane (PDMS), polymethyl methacrylate (PMMA), epoxy resin, and sandwich structure of the top evaporated thin SiO_2 layer with epoxy support.

PDMS was chosen as the first candidate for the substrate for its wide application in the fabrication and prototyping of microfluidic chips. Additionally, it has desired properties such as excellent optical transparency in the visible region, high flexibility, and chemical stability.[44] PDMS casting was done over the sample in a mould.[45] PDMS was prepared from a two-component elastomer kit SYLGARD 184 (Dow) with a weight ratio of 1:10 (curing agent to base). These compounds were thoroughly mixed, and then the solution was degassed either in vacuum or by centrifugation based on the processed volume.

Epoxy resin has a much better thermal stability (thermoset), exceptional adhesion to AuNPs, and good chemical resistance. Like PMMA, its high rigidity is inconvenient for mechanical machining; however, the biggest drawback is a weak resistance to oxygen plasma cleaning, resulting in a limited cleanability of AuNPs. Epoxy casting was done similarly to PDMS casting. Two compound epoxy resin Elan-tron® EC 570 and W 363 with a weight ratio of 100:33 was used as a base material. After mixing, the solution was quickly degassed by centrifugation for 1 min at 2500 RPM. The application over AuNP samples is the same as for PDMS. The epoxy resin was cast in a frame over the AuNP sample to a thickness of a few millimetres and cured for 12 h at 50 °C in an oven. After casting, Kapton tape was applied on the top side of the epoxy against the sample to protect it from chemical damage during the Al removal. Then, the Al substrate was removed.

SiO_2 has ideal properties, including perfect chemical stability as well as resistance to O_2 plasma. The setback is just more advanced requirements for the deposition. A SiO_2 layer of 500 nm was deposited over the AuNP layer in the evaporator setup. The deposition rate was gradually increased, starting with 0.1–0.2 $nm\,s^{-1}$ for the first 50 nm and then up to 2 $nm\,s^{-1}$ for the rest of the deposition. Since the SiO_2 layer is too thin to act as a

free-standing support for the AuNP layer, a thick epoxy layer was cast over it. Afterwards, the Al substrate was removed.

Standard Al removal procedure: The Al substrate was immersed in hydrochloric acid (HCl, 35 % w/w) and 1 M copper(II) chloride ($CuCl_2$) water solution. When the gas evolution stops, the etching is finished, and the sample is pulled out and thoroughly rinsed in tap water, followed by washing in deionized water. Afterwards, it was subsequently immersed into 1 M iron(III) chloride ($FeCl_3$) water solution and 1 M sodium hydroxide (NaOH) water solution for 10 min to remove copper and aluminium oxide residues, respectively. After the etching procedure, the sample was thoroughly washed in deionized water and dried by nitrogen stream.

After transfer, samples were usually cut to smaller pieces with an AuNP layer area of at least 10 mm×10 mm. PDMS samples were cut by a razor, while epoxy samples were cut off by a precision saw (Accutom 100) and then washed by ultra-sonication in deionized water for 2 min. The resulting samples (examples shown in Figure 2.6) have blue colour indirect transmission from the LSPR absorbance peak of AuNPs at 580–600 nm. In refraction, they show a metallic gloss similar to a compact gold film.

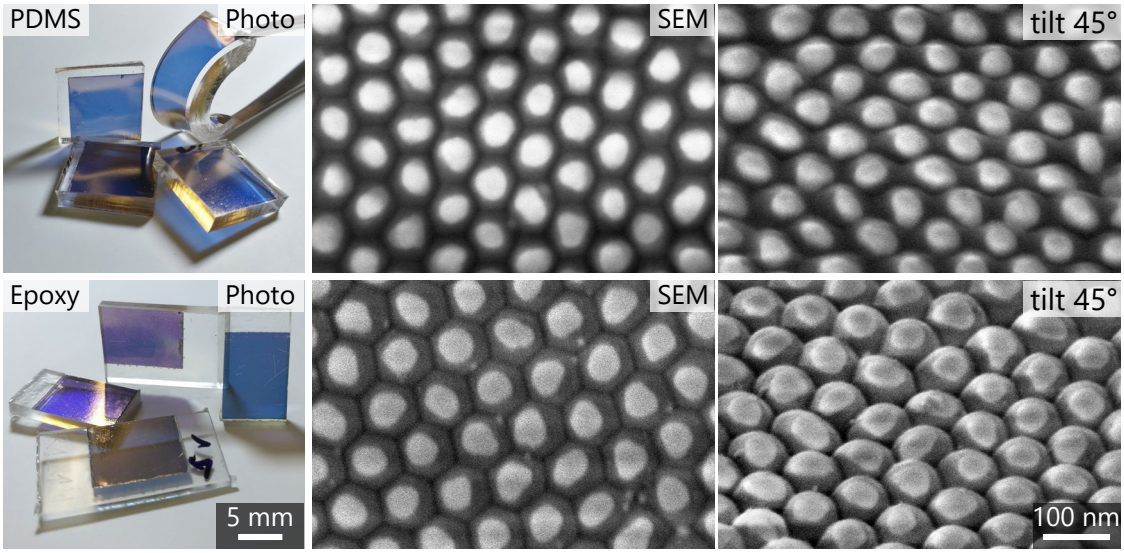

Figure 2.6: Photographs and SEM images of transferred AuNP layers on PDMS and epoxy substrates.

Figure 2.6 shows examples of transferred AuNP layers. In general, the resulting morphology consists of AuNPs on top of the substrate, more or less embedded in hemispherical domes. For PMMA, epoxy, and SiO_2 substrates, embedding is almost perfect, forming very sharp boundaries between the domes. Meanwhile, in the case of PDMS, a smooth wave-like surface is observed. This smoothing may result from either poor wetting performance, migration of PDMS oligomers (discussed later), or an effect of the observation technique (SEM).

2.2.5 AuNPs substrate etching and characterization

As presented in the previous subsection 2.2.4, the AuNP layers can be successfully transferred to various substrates while preserving their initial arrangement. However, due to the technological aspects of the transfer, AuNPs are by large part immersed in their new substrate. The drawback of this configuration is that the surrounding substrate significantly obstructs another medium to access the surface or space between AuNPs, inhibiting the bulk RI sensitivity and DNA hybridization. This section demonstrates a solution in the form of controlled substrate removal around AuNPs that results in a massive increase of sensitivity and the accessibility of AuNP surface for potential modification.

The removal of all substrates was done by plasma reactive ion etching to ensure reasonable control and homogeneity of the process. Additionally, the properties of the selected samples are characterized using SEM/STEM, AFM, XPS, and VIS spectroscopy. The LSPR sensors were successfully used for the label-free detection of a 20 bp long DNA molecule. The DNA detection was done in collaboration with Dr Attila Bonyár, and the results can be found in the attached collaborative article [28].

This section describes the final fabrication step and summarizes the whole development of the LSPR sensor and its fabrication. Only two (epoxy and SiO_2) of four substrate materials are presented in this short version. The comparison is predominantly shown on the AuNP layer formed over 40 V templates by 1st cycle dewetting with a diameter of 65 nm (if not mentioned otherwise).

RIE of the substrate through AuNP layers

Conveniently, the etching progress of all substrates over the AuNP layer can be observed by a visible change of the sample colour. In general, the embedded AuNP layers have strong absorbance peak maxima around 600 nm, which gives them a bluish look in transmitted white light. This effect is illustrated in Figure 2.7, showing the absorption spectra of various etched epoxy samples. With the removal of the surrounding material, the effective bulk RI of the AuNP medium decreases, resulting in a blue shift of AuNP plasmonic resonance with the corresponding change of the sample colour from blue through purple to pink (insets of Figure 2.7).

This fundamental principle of SPR sensing elements can also be used to monitor sample sensitivity by simple colour change observation by immersing part of the sample into a liquid (Figure 2.7). With RI of liquid higher than air and close to the substrate, the colour change reverses back to a bluish one.

Epoxy reactive ion etching (RIE) was performed in a PlasmaPro 80 RIE chamber (Oxford Instruments Plasma Technology), which uses capacitively coupled plasma (CCP).[46] The process parameters were: power of 50 W, the pressure of 6.7 Pa, and 50 sccm of O_2.

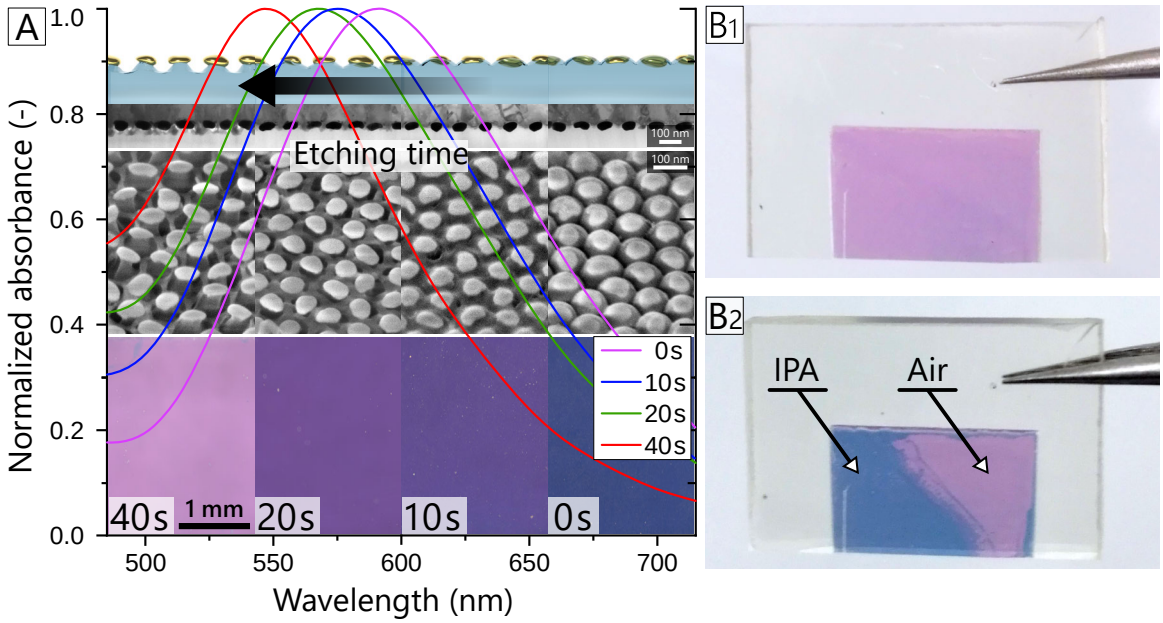

Figure 2.7: (A) The effect of selective substrate etching on normalized absorption spectra of AuNP layers on the epoxy substrate after the different number of repetitions of selective epoxy etching with O_2 plasma measured in air with the inset containing 3D illustration, STEM, SEM and optical microscopy images (transmission) of corresponding samples. The change of colour caused by IPA droplet on substrate etched AuNP layer (A) before and (B) after application.

The overetching time was estimated to be approximately 60 s. Different etch time was selected to investigate the effect of etching in detail by the SEM and STEM (Figure 2.7).

The sample without any etching shows a recognizable epoxy array of spherical caps with embedded AuNPs (SEM). Embedding is better visualized by STEM cross-sections, while AFM images and profiles give better insight into the topography. As can be noted, the height of spherical caps is about 16 nm, which is smaller when compared to the corresponding Al template with a protrusion height of 22 nm. This topological effect is a standard AFM artefact caused by the probe shape (tip radius of 2–12 nm with a tip angle of 40 °C), which cannot perfectly trace over narrow and deep surface features.

After the first 10 s of etching, the substrate is primarily removed from the top sides and periphery of AuNPs. It can be seen on AFM images where the hemispherical topography is lost, revealing protruded AuNPs. The height of the protruding parts is 33 nm, and in this case, approximately the same as the AuNPs height (30.7 ± 3.8 nm). With additional etching, the substrate removal is going into more depth with simultaneous undereching of AuNPs. This process forms the characteristic mushroom-like structure with AuNP on top of a conical epoxy pillar (SEM/STEM: 40 s). The height of the structures for the 30 s etched sample (AFM), and similarly, the 30 s etched sample (STEM) is approximately twice as big as the AuNP thickness. The etching rate can be roughly estimated from AFM measurement to 1.6 nm s^{-1}.

Parallel optical spectrophotometry measurements were done on the same samples.

The normalized absorbance spectra (Figure 2.7) confirmed the successful removal of the surrounding epoxy. The absorbance peak maxima measured in the air decreased from the initial 590 nm to 575, 567.5, and 547 nm after 10, 20, and 40 s etchings, respectively. The changes in the colour of the samples upon etching are visible to the naked eye as well (inset of Figure 2.7). As shown in Figure 2.8:B, this change goes hand in hand with the increase of bulk RI sensitivity, from the initial 15 nm RIU^{-1} to around 80 nm RIU^{-1}, for this particular type of AuNP layer (diameter 65 nm, pitch 105 nm).

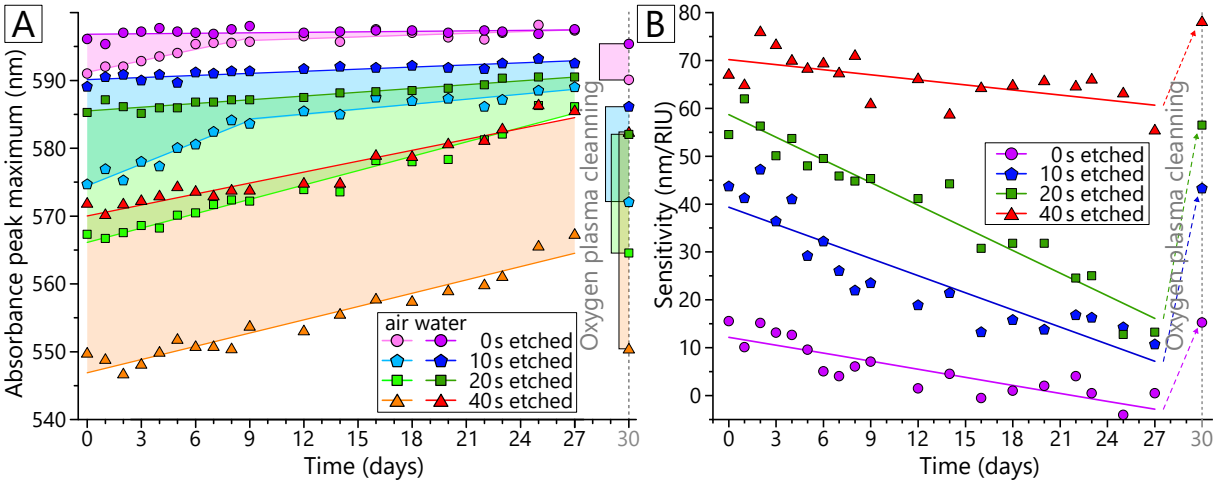

Figure 2.8: (A) Position of the LSPR absorbance peak maxima of the etched nanocomposite samples (Figure 2.7) measured in air ($n = 1$) and water ($n = 1.33$). (B) Calculated bulk RI sensitivities of the same samples. The values on the right side of the graph represent the condition of the samples after cleaning them with low-power O_2 plasma after 30 days. Plasma cleaning was performed in a low-pressure plasma chamber (Tetra 30, Diener) at the pressure of 40 Pa and power of 20 W in an oxygen atmosphere for 15 s.

SiO_2 substrate for AuNPs and its application is included in this work as a proof of concept. The possibility to clean samples by oxygen plasma to any extent without damaging the structures right before or even after selective SiO_2 etching is an excellent advantage of this configuration.

The samples were cleaned before selective etching by oxygen plasma for 1 min at 100 W, 13.3 Pa, 20 sccm (O_2) in the same chamber. This cleaning reduces the uncertainty of etching introduced by surface contamination. The process parameters were: power of 100 W, the pressure of 4.0 Pa, and 50 sccm of $Ar : CHF_3 : O_2$ (6 : 3 : 1). This recipe resulted in preferentially isotropic etching of the structures, as shown in Figure 2.9:A.

The etched samples show great sensitivity (Figure 2.9:C), almost 100 % higher than an epoxy substrate using the same AuNP arrangement. Moreover, the stability of the samples was exceptional without any signs of wear due to NP washing.

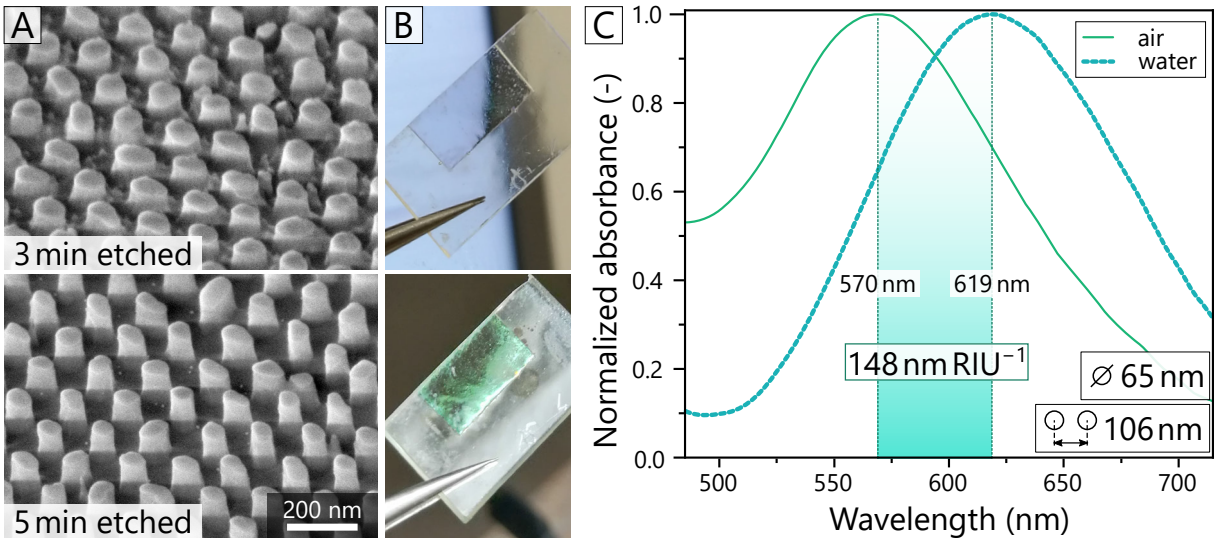

Figure 2.9: (A) SEM images of variously etched AuNPs on a SiO_2 sample. (B) Photos of 5 min etched sample in the transmission and reflection view with (C) normalized absorption spectra of a 3 min etched sample measured in air and water.

2.3 Conclusions and future outlook

This part of the thesis presented a fabrication technology that uses porous anodic alumina (PAA) to form a well-ordered gold nanoparticle layer transferred to a transparent substrate to be utilized for plasmonic sensor applications.

Experimental results in this thesis are structured according to fabrication technology with mini theoretical sections for the selected techniques. After the fabrication of aluminium templates, the fabrication of gold nanoparticles (AuNPs) is explained, showing the crucial aspects of AuNP formation, displacement and size control. It was extensively demonstrated that with this versatile, nanopatterned template-based fabrication technology, large-scale and relatively cheap production with tunable properties is possible. The main advantage of the proposed fabrication technology is the homogeneity of the nanoparticle size/distribution over a large (several cm^2) surface area.

Afterwards, the AuNP layers were transferred onto transparent dielectric substrates to utilize their properties as a plasmonic sensor fully. A reliable technique that sacrifices the Al template was presented with an additional selective etching of the substrate. This selective etching not only changes the AuNP substrate but also modifies its morphology, giving these nanocomposite layers their characteristic mushroom-like structure with lentil-shaped AuNPs on top of conical substrate pillars.

Through some complications in the development, working LSPR sensors based on an epoxy substrate were successfully prepared and characterized. The nanocomposite layers show exceptional sensitivity in comparison to the previous PDMS concepts. This work demonstrated an increase of sensitivity due to selective etching as well as long-

term stability of those layers with successful cleaning, providing reproducible sensitivity. These LSPR sensors were successfully used for the label-free detection of a 20 bp long DNA molecule,[28] performed by Dr Attila Bonyár, making it one of the first NP-polymer surface nanocomposite sensors ever demonstrated for the plasmonic detection of DNA.

Additionally, this work includes the progress that has been made by introducing SiO_2 as a carrier layer for AuNPs. These LSPR sensors offer an almost 100 % increase in sensitivity and improved long-term stability compared to the previous epoxy-based samples. They also do not suffer from degradation during the O_2 plasma cleaning procedures.

In summary, the AuNPs fabrication technique demonstrated in this work represents a robust and scalable technology that allows fine-tuning and optimization of AuNP layer absorption spectra for plasmonic applications such as LSPR and SERS. A significant advantage of this technology is its relatively low cost and that it only includes solid-state processes, while it does not rely on any lithographic processes. Thus, this technique represents a link between randomly arranged nanoparticles formed by, e.g., SSD of thin metallic film or NPs deposited from colloids, and fully controlled arrangements done by, e.g., electron beam lithography (EBL), focused ion beam (FIB), nanoimprint lithography (NIL).

Even though this fabrication method shows remarkable results, it still suffers from a few drawbacks. One of them is the transfer of AuNPs from templates that require the dissolution of the template. Finding a method to separate an AuNP layer and save an underlying template would be the most considerable improvement. It would not be necessary to prepare a fresh Al template for each AuNP layer, and each AuNP layer will be identical. This single step would also make a breakthrough in other methods of AuNPs fabrication. The second drawback is the large-scale order of the defect-free domain size that is limited (to several microns) by the nature of pore nucleation during anodising and PAA growth. Without artificial methods such as lithography, increasing the self-order would be a giant leap proportionate to the first discovery of self-order of PAA.

The future work will include utilizing the recent SiO_2 layer to improve the performance and stability of AuNP layers. Additional performance can also be possibly achieved by optimizing AuNPs that are more focused on specific applications. Additional task will be to understand better the behaviour of PDMS and its possible utilization as a flexible substrate. Besides these, a big challenge will be to find or develop an AuNP transfer technique that will not damage the primary template. The last and probably most challenging to tackle will be improved large-scale self-ordering of PAA formed on an aluminium sheet or even thin deposited layers.

REFERENCES

[1] J. C. Alexander, *Surface Modifications and Growth of Titanium Dioxide for Photo-Electrochemical Water Splitting*, ser. Springer Theses November. Cham: Springer International Publishing, 2016, ISBN: 978-3-319-34227-6.

[2] J. Macak, H. Tsuchiya, A. Ghicov, K. Yasuda, R. Hahn, S. Bauer, and P. Schmuki, 'TiO_2 nanotubes: Self-organized electrochemical formation, properties and applications,' *Curr. Opin. Solid State Mater. Sci.*, vol. 11, no. 1-2, pp. 3–18, Feb. 2007, ISSN: 13590286.

[3] Y. Cai and Y. P. Feng, 'Review on charge transfer and chemical activity of TiO_2: Mechanism and applications,' *Prog. Surf. Sci.*, vol. 91, no. 4, pp. 183–202, Dec. 2016, ISSN: 00796816.

[4] U. Diebold, 'The surface science of titanium dioxide,' *Surf. Sci. Rep.*, vol. 48, no. 5, pp. 53–229, 2003, ISSN: 01675729.

[5] T. Jafari, E. Moharreri, A. Amin, R. Miao, W. Song, and S. Suib, 'Photocatalytic Water Splitting–The Untamed Dream: A Review of Recent Advances,' *Molecules*, vol. 21, no. 7, p. 900, Jul. 2016, ISSN: 1420-3049.

[6] C. McCullagh, J. M. C. Robertson, D. W. Bahnemann, and P. K. J. Robertson, 'The application of TiO_2 photocatalysis for disinfection of water contaminated with pathogenic micro-organisms: a review,' *Res. Chem. Intermed.*, vol. 33, no. 3-5, pp. 359–375, Mar. 2007, ISSN: 0922-6168.

[7] K. Huo, B. Gao, J. Fu, L. Zhao, and P. K. Chu, 'Fabrication, modification, and biomedical applications of anodized TiO_2 nanotube arrays,' *RSC Adv.*, vol. 4, no. 33, p. 17 300, 2014, ISSN: 2046-2069.

[8] M. Marik, A. Mozalev, J. Hubalek, and M. Bendova, 'Resistive switching in TiO_2 nanocolumn arrays electrochemically grown,' *J. Phys. Conf. Ser.*, vol. 829, no. 1, p. 012 001, Apr. 2017, ISSN: 1742-6588.

[9] M. Lohrengel, 'Thin anodic oxide layers on aluminium and other valve metals: high field regime,' *Mater. Sci. Eng. R Reports*, vol. 11, no. 6, pp. 243–294, Dec. 1993, ISSN: 0927796X.

[10] M. Bendova, J. Kolar, F. Gispert-Guirado, and A. Mozalev, 'Porous-Alumina-Assisted Growth of Nanostructured Anodic Films on Tiâ'Nb Alloys,' *ChemElectroChem*, vol. 5, no. 19, pp. 2825–2835, Oct. 2018, ISSN: 21960216.

[11] M. Bendova, J. Kolar, M. Marik, T. Lednicky, and A. Mozalev, 'Influence of nitrogen species on the porous-alumina-assisted growth of TiO_2 nanocolumn arrays,' *Electrochim. Acta*, vol. 281, pp. 796–809, Aug. 2018, ISSN: 00134686.

[12] I. Gablech, V. Svatoš, O. Caha, M. Hrabovský, J. Prášek, J. Hubálek, and T. Šikola, 'Preparation of (001) preferentially oriented titanium thin films by ion-beam sputtering deposition on thermal silicon dioxide,' *J. Mater. Sci.*, vol. 51, no. 7, pp. 3329–3336, Apr. 2016, ISSN: 0022-2461.

[13] G. C. Schwartz, 'An Anodic Process for Forming Planar Interconnection Metallization for Multilevel LSI,' *J. Electrochem. Soc.*, vol. 122, no. 11, p. 1508, 1975, ISSN: 00134651.

[14] T. W. Clyne and S. C. Troughton, 'A review of recent work on discharge characteristics during plasma electrolytic oxidation of various metals,' *Int. Mater. Rev.*, vol. 64, no. 3, pp. 127–162, Apr. 2019.

[15] C. Dunleavy, I. Golosnoy, J. Curran, and T. Clyne, 'Characterisation of discharge events during plasma electrolytic oxidation,' *Surf. Coatings Technol.*, vol. 203, no. 22, pp. 3410–3419, Aug. 2009.

[16] R. Asahi, T. Morikawa, H. Irie, and T. Ohwaki, 'Nitrogen-Doped Titanium Dioxide as Visible-Light-Sensitive Photocatalyst: Designs, Developments, and Prospects,' *Chem. Rev.*, vol. 114, no. 19, pp. 9824–9852, Oct. 2014, ISSN: 0009-2665.

[17] Y. J. Jin, J. Linghu, J. Chai, C. S. Chua, L. M. Wong, Y. P. Feng, M. Yang, and S. Wang, 'Defect Evolution Enhanced Visible-Light Photocatalytic Activity in Nitrogen-Doped Anatase TiO_2 Thin Films,' *J. Phys. Chem. C*, vol. 122, no. 29, pp. 16 600–16 606, Jul. 2018, ISSN: 1932-7447.

[18] J. A. Seabold and K.-S. Choi, 'Effect of a Cobalt-Based Oxygen Evolution Catalyst on the Stability and the Selectivity of Photo-Oxidation Reactions of a WO_3 Photoanode,' *Chem. Mater.*, vol. 23, no. 5, pp. 1105–1112, Mar. 2011, ISSN: 0897-4756.

[19] I. Milošv, H.-H. Strehblow, B. Navinšek, and M. Metikoš-Huković, 'Electrochemical and thermal oxidation of TiN coatings studied by XPS,' *Surf. Interface Anal.*, vol. 23, no. 7-8, pp. 529–539, Jul. 1995, ISSN: 0142-2421.

[20] M. Diamanti, S. Codeluppi, A. Cordioli, and M. Pedeferri, 'Effect of thermal oxidation on titanium oxides' characteristics,' *J. Exp. Nanosci.*, vol. 4, no. 4, pp. 365–372, Dec. 2009, ISSN: 1745-8080.

[21] M. L. Vera, M. R. Rosenberger, C. E. Schvezov, and A. E. Ares, 'Fabrication of TiO_2 Crystalline Coatings by Combining Ti-6Al-4V Anodic Oxidation and Heat Treatments,' *Int. J. Biomater.*, vol. 2015, pp. 1–9, 2015, ISSN: 1687-8787.

[22] J. R. Birch and T. D. Burleigh, 'Oxides Formed on Titanium by Polishing, Etching, Anodizing, or Thermal Oxidizing,' *CORROSION*, vol. 56, no. 12, pp. 1233–1241, Dec. 2000, ISSN: 0010-9312.

[23] D. A. H. Hanaor and C. C. Sorrell, 'Review of the anatase to rutile phase transformation,' *J. Mater. Sci.*, vol. 46, no. 4, pp. 855–874, Feb. 2011, ISSN: 0022-2461.

[24] Y. Liu, F. Ren, G. Cai, M. Hong, W. Li, X. Xiao, W. Wu, and C. Jiang, 'Fabrication of TiO_2 Nanofilm Photoelectrodes on Ti Foil by Ti Ion Implantation and Subsequent Annealing,' *Adv. Condens. Matter Phys.*, vol. 2014, pp. 1–7, 2014, ISSN: 1687-8108.

[25] M. Jarosz, K. Syrek, J. Kapusta-Kołodziej, J. Mech, K. Małek, K. Hnida, T. Łojewski, M. Jaskuła, and G. D. Sulka, 'Heat Treatment Effect on Crystalline Structure and Photoelectrochemical Properties of Anodic TiO_2 Nanotube Arrays Formed in Ethylene Glycol and Glycerol Based Electrolytes,' *J. Phys. Chem. C*, vol. 119, no. 42, pp. 24 182–24 191, Oct. 2015, ISSN: 1932-7447.

[26] E. Petryayeva and U. J. Krull, 'Localized surface plasmon resonance: Nanostructures, bioassays and biosensing—A review,' *Anal. Chim. Acta*, vol. 706, no. 1, pp. 8–24, Nov. 2011, ISSN: 00032670.

[27] Y.-C. Yeh, B. Creran, and V. M. Rotello, 'Gold nanoparticles: preparation, properties, and applications in bionanotechnology,' *Nanoscale*, vol. 4, no. 6, pp. 1871–1880, Mar. 2012, ISSN: 2040-3364.

[28] T. Lednický and A. Bonyár, 'Large Scale Fabrication of Ordered Gold Nanoparticle-Epoxy Surface Nanocomposites and Their Application as Label-Free Plasmonic DNA Biosensors,' *ACS Appl. Mater. Interfaces*, vol. 12, no. 4, pp. 4804–4814, Jan. 2020, ISSN: 1944-8244.

[29] Y. Ozaki, K. Kneipp, and R. Aroca, *Frontiers of Surface-Enhanced Raman Scattering*, Y. Ozaki, K. Kneipp, and R. Aroca, Eds. Chichester, UK: John Wiley & Sons, Ltd, Mar. 2014, vol. 9781118359, pp. 1–313, ISBN: 9781118703601.

[30] A. Bonyár, I. Csarnovics, M. Veres, L. Himics, A. Csik, J. Kámán, L. Balázs, and S. Kökényesi, 'Investigation of the performance of thermally generated gold nanoislands for LSPR and SERS applications,' *Sensors Actuators B Chem.*, vol. 255, pp. 433–439, Feb. 2018, ISSN: 09254005.

[31] M. P. Raphael, J. A. Christodoulides, J. B. Delehanty, J. P. Long, P. E. Pehrsson, and J. M. Byers, 'Quantitative LSPR Imaging for Biosensing with Single Nanostructure Resolution,' *Biophys. J.*, vol. 104, no. 1, pp. 30–36, Jan. 2013, ISSN: 00063495.

[32] H. M. Jin, J. Y. Kim, M. Heo, S.-J. Jeong, B. H. Kim, S. K. Cha, K. H. Han, J. H. Kim, G. G. Yang, J. Shin, and S. O. Kim, 'Ultralarge Area Sub-10 nm Plasmonic Nanogap Array by Block Copolymer Self-Assembly for Reliable High-Sensitivity SERS,' *ACS Appl. Mater. Interfaces*, vol. 10, no. 51, pp. 44 660–44 667, Dec. 2018, ISSN: 1944-8244.

[33] N. D. Israelsen, C. Hanson, and E. Vargis, 'Nanoparticle Properties and Synthesis Effects on Surface-Enhanced Raman Scattering Enhancement Factor: An Introduction,' *Sci. World J.*, vol. 2015, pp. 1–12, 2015, ISSN: 2356-6140.

[34] T. Lednický, 'Template Assisted Electrodeposition of Multilayer Nanostructures,' Master's Thesis, Brno University of Technology, 2014, p. 83, ISBN: 0824758498.

[35] S. Yang, F. Xu, S. Ostendorp, G. Wilde, H. Zhao, and Y. Lei, 'Template-confined dewetting process to surface nanopatterns: Fabrication, structural tunability, and structure-related properties,' *Adv. Funct. Mater.*, vol. 21, no. 13, pp. 2446–2455, 2011, ISSN: 1616301X.

[36] W. Yingwei, W. Fei, F. Liping, F. Jingyue, W. Guang, C. Shengli, and Z. Xueao, 'Self-assembled Au nanoparticles arrays by porous anodic alumina oxide and optical properties,' *Infrared Laser Eng.*, vol. 42, no. 11, pp. 3047–3052, Nov. 2013, ISSN: 1007-2276.

[37] H. Jo, D. Yoon, A. Sohn, D.-W. Kim, Y. Choi, T. Kang, D. Choi, S.-W. Kim, and L. P. Lee, 'Asymmetrically Coupled Plasmonic Core and Nanotriplet Satellites,' *J. Phys. Chem. C*, vol. 118, no. 32, pp. 18 659–18 667, Aug. 2014, ISSN: 1932-7447.

[38] M. Altomare, N. T. Nguyen, and P. Schmuki, 'Templated dewetting: designing entirely self-organized platforms for photocatalysis,' *Chem. Sci.*, vol. 7, no. 12, pp. 6865–6886, 2016, ISSN: 20416539.

[39] A. Bonyár, T. Lednický, and J. Hubálek, 'LSPR Nanosensors with Highly Ordered Gold Nanoparticles Fabricated on Nanodimpled Aluminium Templates,' *Procedia Eng.*, vol. 168, pp. 1160–1163, Jan. 2016, ISSN: 18777058.

[40] X. Fan, Q. Hao, R. Jin, H. Huang, Z. Luo, X. Yang, Y. Chen, X. Han, M. Sun, Q. Jing, Z. Dong, and T. Qiu, 'Assembly of gold nanoparticles into aluminum nanobowl array,' *Sci. Rep.*, vol. 7, no. 1, p. 2322, Dec. 2017, ISSN: 2045-2322.

[41] H. Ikeda, M. Iwai, D. Nakajima, T. Kikuchi, S. Natsui, N. Sakaguchi, and R. O. Suzuki, 'Nanostructural characterization of ordered gold particle arrays fabricated via aluminum anodizing, sputter coating, and dewetting,' *Appl. Surf. Sci.*, vol. 465, pp. 747–753, Jan. 2019, ISSN: 01694332.

[42] X. Sun and H. Li, 'Gold nanoisland arrays by repeated deposition and post-deposition annealing for surface-enhanced Raman spectroscopy,' *Nanotechnology*, vol. 24, no. 35, p. 355 706, Sep. 2013, ISSN: 0957-4484.

[43] M. Kang, S.-G. Park, and K.-H. Jeong, 'Repeated Solid-state Dewetting of Thin Gold Films for Nanogap-rich Plasmonic Nanoislands,' *Sci. Rep.*, vol. 5, no. 1, p. 14 790, Dec. 2015, ISSN: 2045-2322.

[44] U. Eduok, O. Faye, and J. Szpunar, 'Recent developments and applications of protective silicone coatings: A review of PDMS functional materials,' *Prog. Org. Coatings*, vol. 111, pp. 124–163, Oct. 2017, ISSN: 03009440.

[45] J. Friend and L. Yeo, 'Fabrication of microfluidic devices using polydimethylsiloxane,' *Biomicrofluidics*, vol. 4, no. 2, p. 026 502, Jun. 2010, ISSN: 1932-1058.

[46] S. M. Rossnagel, J. J. Cuomo, and W. D. W. D. Westwood, *Handbook of plasma processing technology : fundamentals, etching, deposition, and surface interactions*. Noyes Publications, 1990, p. 523, ISBN: 9780815512202.

A LIST OF AUTHOR'S SCIENTIFIC ACHIEVEMENTS

Author's scientific identifiers

Researcher ID:	AAE-6679-2020
ORCID ID:	0000-0003-0564-1862
SCOPUS ID:	57188768803

A.1 Publications in impact journals

1. **Lednický, T.**; Bonyár, A. 'Large Scale Fabrication of Ordered Gold Nanoparticle-Epoxy Surface Nanocomposites and Their Application as Label-Free Plasmonic DNA Biosensors' *ACS Applied Materials and Interfaces*, vol. 12, no. 4, 2020, pp. 4804–4814. doi:10.1021/acsami.9b20907.

   ISSN 1944-8244. Impact factor (2019): 8.758.

   My contribution: fabrication of samples, design of experiments, sample preparation, measurements and evaluation of experiments (except detection of DNA hybridization), partially writing the manuscript.

2. Simunkova, H.; **Lednický, T.**; Whitehead, A.H.; Kalina, L.; Simunek, P.; Hubalek, J. 'Tantalum-based nanotube arrays via porous-alumina-assisted electrodeposition from ionic liquid: Formation and electrical characterization', *Applied Surface Science*, vol. 548, no. 9, 2021, pp. 149264. doi:10.1016/j.apsusc.2021.149264.

   ISSN 0169-4332. Impact factor (2019): 6.182.

   My contribution: SEM measurements and design of experiments, revision of the manuscript.

3. Vallejos Vargas, S.; Grácia, I.; **Lednický, T.**; Vojkůvka, L.; Figueras, E.; Hubálek, J.; Cané, C. 'Highly hydrogen sensitive micromachined sensors based on aerosol-assisted chemical vapor deposited ZnO rods', *Sensors and Actuators B: Chemical*, vol. 268, 2018, pp. 15–21. doi:10.1016/j.snb.2018.04.033.

   ISSN 0925-4005. Impact factor (2019): 7.100.

   My contribution: XPS measurements and design of experiments, revision of the manuscript.

4. Bendová, M.; Kolář, J.; Márik, M.; **Lednický, T.**; Mozalev, A. 'Influence of nitrogen species on the porous-alumina-assisted growth of TiO_2 nanocolumn arrays.',

Electrochimica Acta, vol. 281, no. 1, 2018, pp. 796–809. doi:10.1016/j.electacta.2018.05.197.

ISSN 0013-4686. Impact factor (2019): 6.215.

My contribution: XPS analyses and the manuscript revision.

5. Bezdekova, J.; Vlcnovska, M.; Zemankova, K.; Bacova, R.; Kolackova, M.; **Lednický, T.**; Pribyl, J.; Richtera, L.; Vanickova, L.; Adam, V.; Vaculovicova, 'Molecularly imprinted polymers and capillary electrophoresis for sensing phytoestrogens in milk', *Journal of Dairy Science*, vol. 103, no. 6, 2020, pp. 4941–4950, doi:10.3168/jds.2019-17367.

   ISSN 0022-0302. Impact factor (2019): 3.333.

   My contribution: XPS measurements, minor manuscript revision.

A.2 Contributions to conference proceedings indexed in WoS or Scopus

1. Zangana, S.; **Lednický, T.**; Rigó, I.; Csarnovics, I.; Veres, M.; Bonyár, A. 'Surface-Enhanced Raman Spectroscopy Investigation of DNA Molecules on Gold/Epoxy Nanocomposite Substrates', *IEEE 26th International Symposium for Design and Technology in Electronic Packaging (SIITME)*, 21–24 October 2020, ISSN: 2642-7036, doi:10.1109/SIITME50350.2020.9292267.

2. **Lednický, T.**; Mozalev, A.; Bendová, M. 'Electrochemical characterization of pure and nitrogen- containing anodic TiO_2 nanocolumn arrays', *8th International Conference on Nanomaterials - Research and Application (NANOCON2016)*, 2017, pp. 669–674, ISBN: 978-80-87294-71-0.

3. Bonyár, A.; **Lednický, T.**; Hubálek, J. 'LSPR Nanosensors with Highly Ordered Gold Nanoparticles Fabricated on Nanodimpled Aluminium Templates', *Procedia Engineering*, vol. 168, 2016, pp. 1160–1163, doi:10.1016/j.proeng.2016.11.390.

4. **Lednický, T.**; Mozalev, A. 'Optimization of Self-organized Growth of Nanoporous Anodic Alumina Templates for Capacitor Application.', *NANOCON 2015: 7th International Conference on Nanomaterials - Research and Application*, 2015, pp. 265–269, ISBN: 978-80-87294-59-8.

A.3 Contributions to conference proceedings and meetings

1. **Lednický, T.**; Plichta, T.; Fohlerová, Z.; Bonyár, A. 'PDMS degradation detection by LSPR of embedded AuNPs array', *18th International Conference on Thin Films & 18th Joint Vacuum Conference*, 22–26 November 2020.

2. **Lednický, T.**; Bonyár, A.; 'Highly-ordered gold nanoparticles surface fabrication for localized surface plasmon resonance sensors', *Curie - Pasteur - CEITEC joint young scientist retreat*, 2017, p. 73.

3. **Lednický, T.**; Bonyár, A.; 'Highly-ordered gold nanoparticle surfaces for localized surface plasmon resonance sensors', *CEITEC PhD Retreat II. Book of abstracts*, 2017, p. 90, ISBN: 978-80-210-8550-3.

4. **Lednický, T.**; Mozalev, A.; Bendová, M. 'Electro- and Photoelectrochemistry on TiO_2-based Nanorod Arrays via Anodizing Al/Ti and Al/TiN_x Layers', *21st Topical Meeting of the International Society of Electrochemistry; Photoelectrochemistry of semiconductors at the nanoscale: from fundamental aspects to practical applications. International Society of Electrochemistry*, 2017, p. 117.

5. **Lednický, T.**; Mozalev, A.; Bendová, M. 'TiO_2-based Nanocolumn Arrays for Photoelectrochemical Water Splitting: Electrochemical Characterization', *International Conference on Advances in Semiconductors and Catalysts for Photoelectrochemical Fuel Production (SolarFuel16)*, 2016.

6. Kynclová, H.; **Lednický, T.**; Hrdý, R.; Prášek, J.; Hubálek, J. 'Gold nanostructured surfaces based on alumina template.', *In XVI. Workshop of Physical Chemists and Electrochemists*, 2016, pp. 101–103, ISBN: 978-80-210-8267-0.

7. **Lednický, T.** 'Solid-state synthesis of gold nanoparticles films for spectroscopic measurement enhancement', *In XVI. Workshop of Physical Chemists and Electrochemists*, 2016, pp. 104–107, ISBN: 978-80-210-8267-0.

8. **Lednický, T.** 'Solid-state Synthesis of Gold Nanoparticles on Dimpled Aluminum Surfaces and Their Transfer to Transparent Substrates', *Proceedings of the 22nd Conference STUDENT EEICT 2016*, 2016, pp. 670–674, ISBN: 978-80-214-5350-0.

9. **Lednický, T.**; Mozalev, A. 'On the growth behavior of nanoporous anodic films on aluminium in citric acid electrolytes', *In Proceedings of the International Con-*

ference on Advances in Electronic and Photonic Technologies (ADEPT 2015), 2015, pp. 202–205, ISBN: 978-80-554-1033-3.

10. **Lednický, T.**; Mozalev, A. 'On the anodizing behaviour of aluminium in citric acid Electrolytes', *XV. Workshop of Physical Chemists and Electrochemists*, 2015, pp. 111–114, ISBN: 978-80-210-7857.

11. **Lednický, T.**; Mozalev, A. 'Effect of pretreatment parameters on the anodizing behaviour of Al foils in citric acid electrolytes', *In CEITEC PhD Retreat, 23-24 April 2015, Valtice, Czech Republic*, 2015, p. 100, ISBN: 978-80-210-7825-3.

12. Kynclová, H.; Majzlíková, P.; Prášek, J.; **Lednický, T.**; Hrdý, R.; Hubálek, J. 'Production and study of nanoporous alumina membranes by electrochemical methods', *47th Heyrovsky Discussion on Electrochemistry of Organic and Bioactive Compounds*, 2014, p. 36, ISBN: 978-80-87351-29-1.